IOP Publishing Journal Title

Journal **XX** (XXXX) XXXXXX https://doi.org/XXXX/XXXX

This is the Accepted Manuscript version of an article accepted for publication in Smart Materials and Structures. IOP Publishing Ltd is not responsible for any errors or omissions in this version of the manuscript or any version derived from it. The Version of Record is available online at https://doi.org/10.1088/1361-665X/abc147.

High strength steel frames with SMA connections in self-centring energy dissipation bays: behaviour insights and a multi-mode-based nonlinear static procedure

Ke Ke[1,2], Michael C.H. Yam[3,4], Huanyang Zhang[1,*], Angus C.C. Lam[5], Xuhong Zhou[1,2]

[1]Hunan Provincial Key Laboratory on Damage Diagnosis for Engineering Structures, Hunan University, Changsha, China
[2] Key Laboratory of New Technology for Construction of Cities in Mountain Area, School of Civil Engineering, Chongqing University, Chongqing, China
[3] Department of Building and Real Estate, The Hong Kong Polytechnic University, Hong Kong, China
[4] Chinese National Engineering Research Centre for Steel Construction (Hong Kong Branch), The Hong Kong Polytechnic University, Hong Kong, China
[5]Department of Civil and Environmental Engineering, University of Macau, Macau, China

E-mail: kerk.ke@outlook.com, michael.yam@polyu.edu.hk, zhanghuanyang@hnu.edu.cn, fstccl@umac.mo, zxh@chd.edu.cn

Received xxxxxx
Accepted for publication xxxxxx
Published xxxxxx

Abstract

This study firstly explores the effectiveness of SMA-based Self-centring Energy Dissipation Bay (SCEDB) for enhancing the seismic performance of high strength steel (HSS) frames. The work is commenced by developing an ensemble of prototype HSS frames equipped with SCEDBs, namely HSSF-SCEDB structures. The prototype systems are analysed under cyclic pushover analyses and nonlinear response history analyses (NL-RHAs). According to the analysis database, it is found that the cyclic pushover responses generally show typical flag shape for a wide deformation range, and the post-earthquake residual deformations are below 0.5% even after experiencing maximum interstorey drifts beyond the codified deformation threshold (i.e. 2%). To offer a practical tool for engineers in damage-control behaviour evaluation and seismic demands estimation, a multi-mode-based nonlinear static procedure based on the modified energy balance concept is developed. Conventional procedures according to the fundamental vibration mode are also revisited. The results indicate that a medium-rise HSSF-SCEDB may be appreciably influenced by higher vibration mode. The difference between average maximum interstorey drifts by NL-RHAs and those by the proposed procedure under an ensemble of earthquake motions is generally below 5%, and the adequacy of the proposed method is justified.

Keywords: High strength steel, Energy dissipation bay, Self-centring, Shape memory alloy, Nonlinear static procedure

Ke, K., Yam, M. C., Zhang, H., Lam, A. C., & Zhou, X. (2020). High-strength steel frames with SMA connections in self-centring energy-dissipation bays: insights and a multimodal nonlinear static procedure. Smart Materials and Structures, 29(12), 125020.

1. Introduction

High strength steels (HSSs) with the nominal yield strength equal or over 460 MPa have recently attracted much attention from both academic and engineering communities [1, 2]. Owing to the higher strength of the material, effective application of HSSs can reduce member section sizes in a steel structure, and hence produces economical and sustainable structures. Although HSS is generally characterised by finite ductility and insignificant post-yielding strain hardening, recent research advances in hysteretic behaviour of HSS materials [3-6], connections/members [7-9] and structural systems [10-19] have shed considerable lights on the promise of their practical implementations in seismic regions. It was confirmed that an effective combination of HSSs and normal steels (e.g. mild carbon steel) in a structure contributes to the formation of desirable damage-control behaviour [15-18, 20] with inelastic actions easily limited to pre-selected members and components for a wide deformation spectrum. For instance, Dubina et al. [11] examined the feasibility of eccentrically-braced HSS frames equipped with ductile shear links, and the advanced damage evolution mode was confirmed. Alternatively, Ke and colleagues have explored the effectiveness of energy dissipation bays [15-18] for enhancing the seismic resistance of a HSS frame. The notion of a HSS frame equipped with energy dissipation bays, i.e. the HSSF-EDBs, is illustrated in figure 1. The satisfactory seismic behaviour of the system including the progressive damaging sequence and the mitigated post-earthquake residual deformation responses in an expected deformation range was confirmed through large-scale quasi-static tests [15, 16].

Nonetheless, the previous research works on HSSF-EDBs generally prioritised the plastic energy dissipation capacity and ductility of the energy dissipation bays, and the energy dissipation mechanisms were based on sacrificial links with plump hysteretic responses. To realise good recentring ability of the structure, a strong HSS frame with sufficient elastic restoring forces is recommended to pull the structure back to the upright position [15, 21]. In addition, for energy dissipation bays installed with conventional ductile links exhibiting full force-displacement responses, the post-earthquake repair works might be costly and complex due to significant permanent residual deformations and residual force sustained by the damaged components as demonstrated in the literature [22, 23]. Therefore, more efforts may be needed towards further seismic performance enhancement of HSS frames.

Recently, innovative "self-centring" technologies enable further advance of seismic design methodology. Apart from using post-tensioned approach to achieve the self-centring behaviour [24-26], research studies indicate that the self-centring behaviour may be realised using Shape Memory Alloys (SMAs) [27-32]. Owing to the superelastic behaviour of SMAs which enables recovery from significant strains (up to 8% to 10%) spontaneously by unloading, novel self-centring connections equipped with superelastic SMA bolts/bars have emerged as promising candidates for steel frame structures. The excellent self-centring performance accompanied by moderate energy dissipation capability of these connections was confirmed by extensive investigations [33-39]. Recently, SMA-based systems are widely being utilised in the steel frame [40-43]. To shed lights on the seismic performance of structures equipped with novel SMA connections, DesRoches et al. [40] examined the seismic responses of steel MRFs incorporating SMA connections based on a numerical study. The results showed that the deformation demand of the MRFs was reduced due to the presence of SMA connections. More recently, Sultana and Youssef [41] observed that the arrangement and the locations of the SMA connections appreciably affect the structural seismic response of MRFs. However, knowledge in optimised application strategies of SMA-based connections in steel frames needs further examination. In addition, quantitative approaches which may be used by practitioners to quantify the inelastic seismic demand of novel steel frames equipped with SMA connections are in urgent need.

Based on the above, the primary objective of this study is to explore the effectiveness of utilising self-centring energy dissipation bays (SCEDBs) equipped with SMA-based connections to enhance the seismic performance of HSS frames. The notion of superelastic-SMA-based SCEDB and the implementation strategy of SCEDBs in HSS frame towards a novel system, namely the HSSF-SCEDB structure, are examined. The seismic performance of a prototype HSSF-SCEDB is examined by cyclic pushover analysis and nonlinear response history analyses (NL-RHAs). The maximum roof displacement, maximum interstorey drift and post-earthquake residual drifts are gathered from the analysis database and examined in detail. The damage-control behaviour and inelastic seismic demand of a damage-control HSSF-SCEDB based on a multi-mode-based nonlinear static procedure are quantified. The adequacy of the proposed method is verified by results from NL-RHAs and comparison against conventional procedures.

2. Implementation of SCEDBs for enhancing HSS frames

In this study, it is proposed to develop a SMA connection based on the work by Ocel et al. [33] as shown in figure 2. The connection adopts superelastic SMA bars to resist the connection moment and high strength bolts installed in the shear tab to resist the applied shear force. According to Ocel et al. [33], the SMA bars buckled at significant deformation

levels, which may affect the connection performance. Thus, the proposed connection utilises a steel buckling restraint (i.e. a steel tube connected with flexible rings) to strengthen the superelastic SMA bars against buckling as shown in figure 2. To concentrate inelastic actions in the SMA bars at large deformations, slot bolt holes are introduced in the shear tab connection, allowing for rotation of the links (figure 2). A demonstration of the validity of the modified connection and a simplified modelling technique will be discussed later.

In this context, a self-centring energy dissipation bay (SCEDB) may be realised by employing the self-centring SMA connections in the energy dissipation bay. In particular, a SCEDB is composed of two HSS columns and links connecting the columns, and self-centring connections discussed above are used to connect the links with the columns. The major functions of the SCEDBs are summarised as follows: (1) The SCEDBs can enhance the lateral stiffness of the entire structure against normal loads (e.g. wind) in the elastic stage and (2) when the structure is pushed to more significant deformations under earthquake motions, "superelastic hinges" at the link-to-column junctions can be triggered, producing both hysteretic energy dissipation and recentring behaviour. Concurrently, the HSS frames may continue to deform in the elastic stage for a wider deformation range. Therefore, a desirable damage-control behaviour limiting the inelastic actions in the SCEDBs may be achieved by an effective combination of SCEDBs and HSS frames.

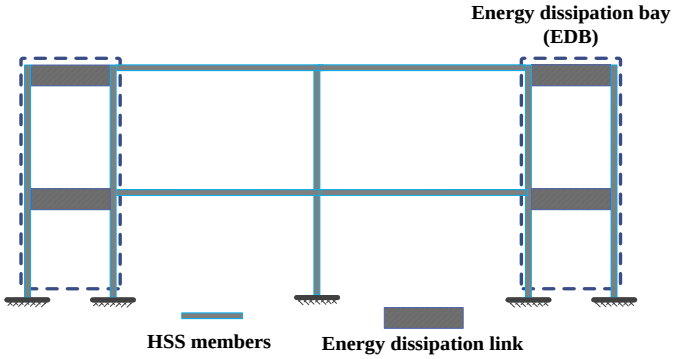

Figure 1. Notion of high strength steel moment resisting frames equipped with energy dissipation bays (HSSF-EDBs) [15, 16].

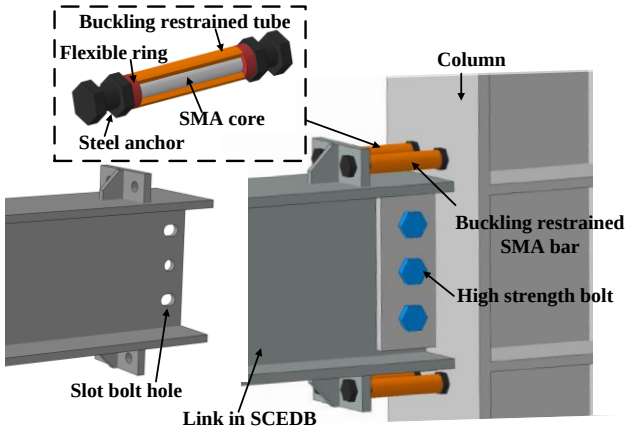

Figure 2. Configuration of the shape memory alloy (SMA) connection.

3. Seismic performance of prototype structures

3.1 Basic information about the prototype structures

To examine the effectiveness of HSSF-SCEDBs for seismic applications, three prototype low-to-medium rise prototype HSSF-SCEDBs are designed according to the Chinese seismic design provisions [44]. Although the trial design does not intend to generate an optimised structure, it has included essential quantities of a HSSF-SCEDB. In particular, one three-storey and two six-storey HSSF-SCEDBs designated as office buildings are designed and to be constructed on sites with stiff soil. The elastic seismic demand for the prototype structures is determined based on design spectra documented in GB50011-2010 (2016) [44].

The layout and the elevation of the prototype systems are shown in figure 3, and the focus of the current study is given to a 2-D frame. For all prototype structures, a dead load of 5 kN/m^2 and a live load of 2.5 kN/m^2 are assumed according to the Chinese load code for design of building structures

(GB5009-2012) [45]. The seismic weight and gravity load are computed by the tributary area as illustrated in figure 3. For the three buildings, HSS with the nominal yield strength of 460 MPa is used to develop the frame members. Two SCEDBs are located at the external bays of the structures, and the SMA connections mentioned in Section 2 are installed in the structure. Six SMA bars with a diameter of 16 mm are preliminarily selected for each connection, and a typical connection for the three-storey structure is given in figure 3(b). To explore the effect of SMA bolt length on the behaviour of the structures, the bolt length of 75 mm and 150 mm are considered in the two 6-storey structures, respectively. As for the material property of SMAs, the "forward transformation start stress (σ^{Ms})" representing inelasticity inception of the material is set as 280 MPa according to the material test results of SMA bars [39]. According to typical configurations of the connections are shown in figure 3(b), the design yield moment of the connections is calculated to be 67.2 kN · m assuming that the rotation centre is in line with the centroid axis of the link. Pin connections are used to connect the SCEDBs to the main HSS frames to increase the elastic deformation range of the HSS frames, as shown in figure 3. The modelling techniques will be discussed in later sections.

3.2 Finite element modelling techniques of the prototype structures

The finite element (FE) software ABAQUS [46] is utilised to model the prototype structures. Two-node linear beam elements (first order interpolation), i.e. B31 elements, are adopted for the columns and the beams in the frame structure. The mesh size for the elastic segment of the members (i.e. the region away from the plastic hinges) is set as 200 mm, whilst the segment expected to experience significant inelastic actions is discretised with a refined mesh (i.e. a size of 50 mm). The bilinear kinematic hysteretic material model with von Mises yield criterion is adopted for the HSS frame members (i.e. beams and columns) with the nominal yield strength of 460 MPa. Rigid joint assumption is applied to the connections in the frames. To produce pin connections in the structures (figure 3), the "Release" option [46] is used to allow for the rotation of the corresponding elements.

As for the SCEDBs, a simplified "nonlinear-spring-based" connection model is developed for the connections equipped with the SMA bolts. Nonlinear axial springs governed by the Auricchio's hysteretic model [47] are used to simulate the behaviour of the superelastic SMA bolts installed in the SCEDBs, and a pin joint is used to simulate the shear tab in the connection. An illustration of the simplified connection model is shown in figure 4(a). The essential parameters of the superelastic SMA materials include the state transformation stresses, i.e. forward transformation start stress (σ^{MS}), forward transformation end stress (σ^{Mf}), reverse transformation start stress (σ^{AS}) and reverse transformation end stress (σ^{Af}), austenite elasticity (E^{A}), martensite elasticity (E^{M}), maximum transformation strain (ε^{L}), and Poisson ratios (ν^{A} and ν^{M}), are based on Fang et al. [39] as shown in figure 4(b) and table 1.

Table 1. SMA material properties used in the FE study [39].

Material properties	Values
Forward transformation start stress σ^{MS}	280 MPa
Forward transformation end stress σ^{Mf}	380 MPa
Reverse transformation start stress σ^{AS}	150 MPa
Reverse transformation end stress σ^{Af}	75 MPa
Austenite elasticity E^{A}	35 GPa
Martensite elasticity E^{M}	25 GPa
Maximum transformation strain ε^{L}	5%
Poisson's Ratio ν^{A}	0.33
Poisson's Ratio ν^{M}	0.33

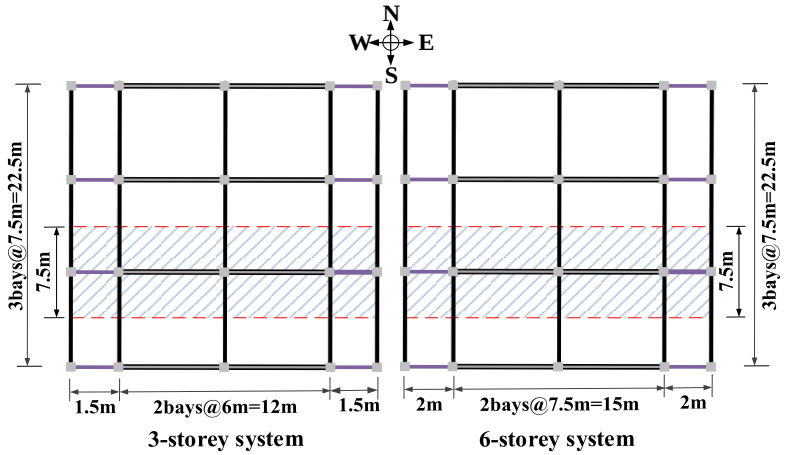

(a)

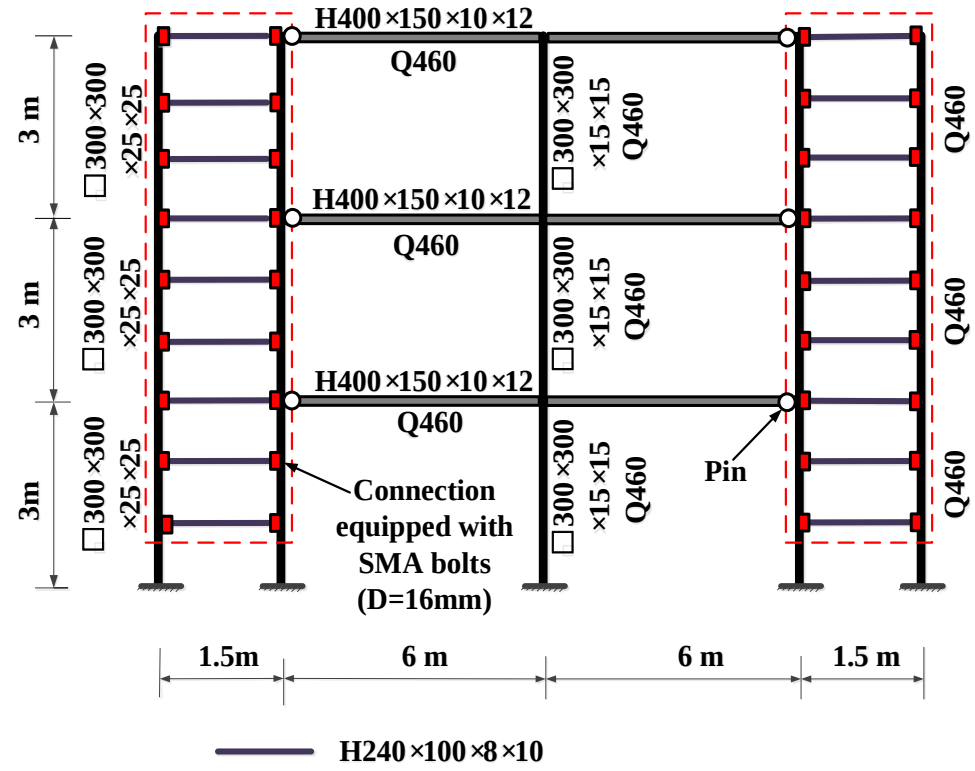
H400×150×10×12
Q460
□300×300×25×25
□300×300×15×15
Q460
3 m
3 m
3m
Connection equipped with SMA bolts (D=16mm)
Pin
1.5m
6 m
6 m
1.5 m
H240×100×8×10

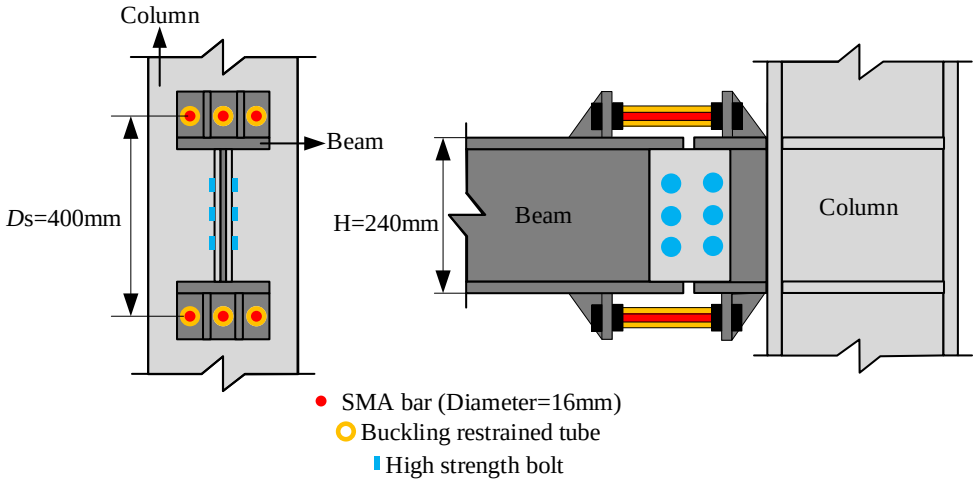
Column
Beam
Ds=400mm
H=240mm
Beam
Column
SMA bar (Diameter=16mm)
Buckling restrained tube
High strength bolt

(b)

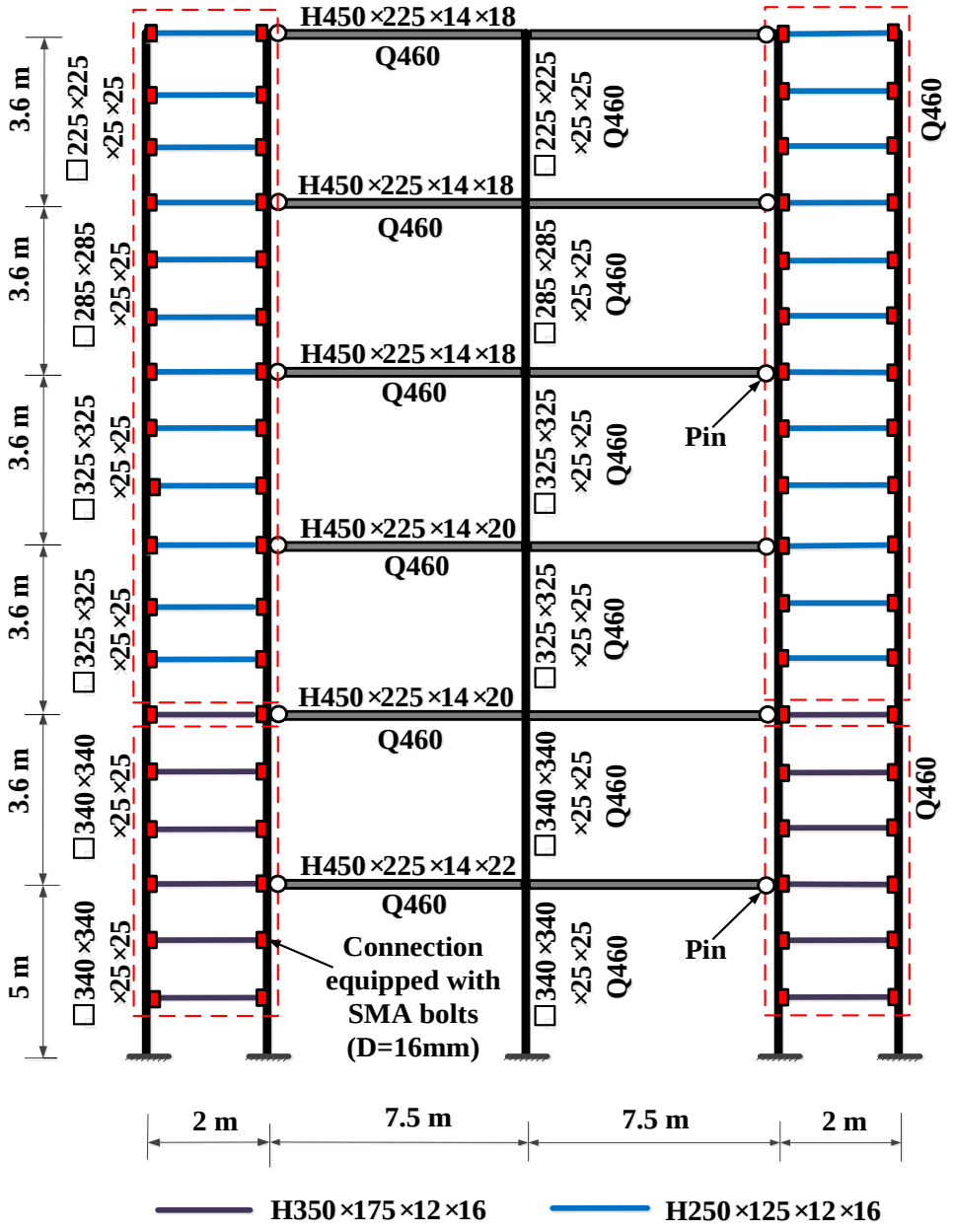

(c)

Figure 3. Structural arrangement of prototype systems: (a) structural layout, (b) 3-storey system and (c) 6-storey system.

3.3 Validation of the modelling techniques

To confirm the adequacy of the nonlinear-spring-based model for reproducing the behaviour of the SMA connection (figure 4(a)), a detailed finite element model of a prototype connection was first established (figure 4(c)). The detailed information on the prototype connection is given in table 2. In the modelling, SMA bars and the buckling restrained tube were modelled using the eight-node linear solid elements (i.e. C3D8 elements). The column stub and the beam stub are discretised by eight-node linear solid elements considering reduced integration (i.e. C3D8R elements). "Hard contact" option that can simulate the contact action in the normal direction accompanied with a "Penalty" friction (the friction coefficient is 0.3 [39]) formulation characterising contacting behaviour in the tangential direction is utilised to model all the contacting surfaces. "Merge" strategy [46] is used to simulate all welded junctions, assuming that no welding failure would occur. For the steel material, the bilinear kinematic hysteretic model governed by von Mises yield criterion is adopted. As for the SMA material, the material properties based on Fang et al. [39] (table 1) are adopted. The detailed FE model of the prototype connection (figure 4(c)) and the nonlinear-spring-based model (figure 4(a)) are

analysed under cyclic loading scenarios, and the good agreement between the moment-rotation responses based on the nonlinear-spring-based model and those by the detailed FE model is demonstrated in figure 4(d). However, to fully verify the modelling techniques, the rationale of the detailed modelling techniques may also need to be confirmed. Thus, the detailed FE modelling techniques mentioned above are applied to replicating the test responses of a SMA-based connection (specimen D8L240) examined by Fang et al. [39] to justify their sufficiency. The overview of the test connection model is shown in figure 4(e), and the accuracy of the modelling is confirmed by comparing the test response curve and predictions by the detailed FE model (figure 4(f)). Note that although the configuration of the test connection (figure 4(e)) is not identical to that of the proposed connection (figure 4(c)), the validation has included essential mechanical characteristics of the prototype connection (i.e. interaction between SMA bolts and structural elements). Thus, the detailed FE modelling techniques may be used to well capture the hysteretic behaviour of the proposed connection, enabling further validation of the nonlinear-spring-based connection model. On the other hand, verifications of the modelling techniques of Q460 HSS frame members, which have been explored in previous works [17], are reproduced in Appendix A.

Table 2. Connections in the validation study.

Connection	Member	Section	Dimension (mm)	Steel grade
Prototype connection	Column	□300×300×25×25	L=2000	Q460
	Beam	H300×200×12×16	L_b=1625	Q460
	SMA bolts	-	L_s=152	-
			D_s=350	
Test connection in [39]	Column	H350×350×16×24	L_c=1292	S355
	Beam	H150×100×10×10	L_b =1025	S355
	SMA bolts	-	L_s=240	-
			D_s=210	

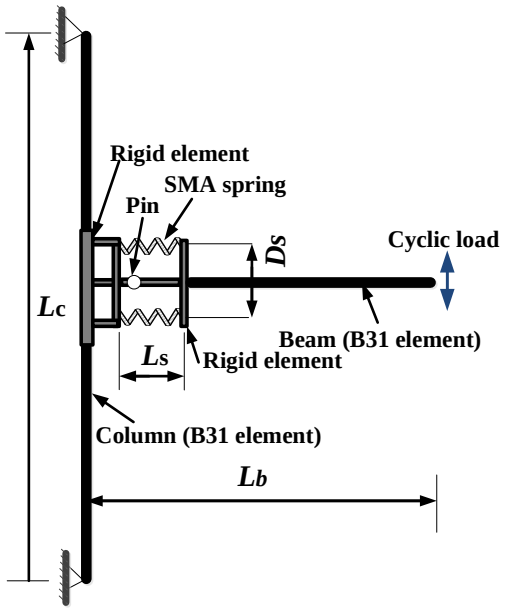

(a)

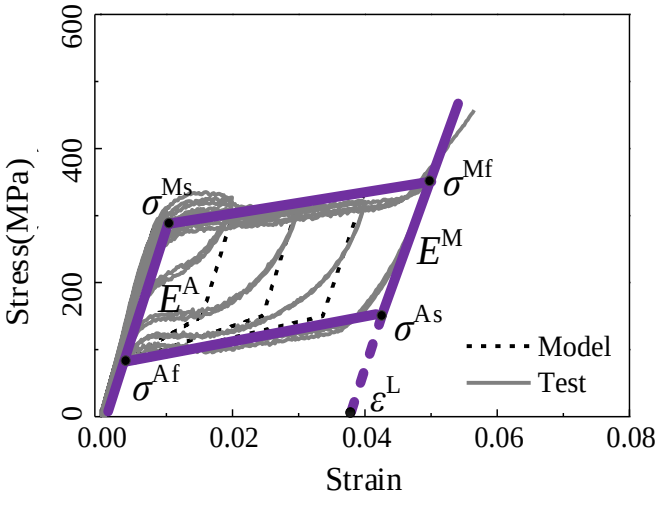

(b)

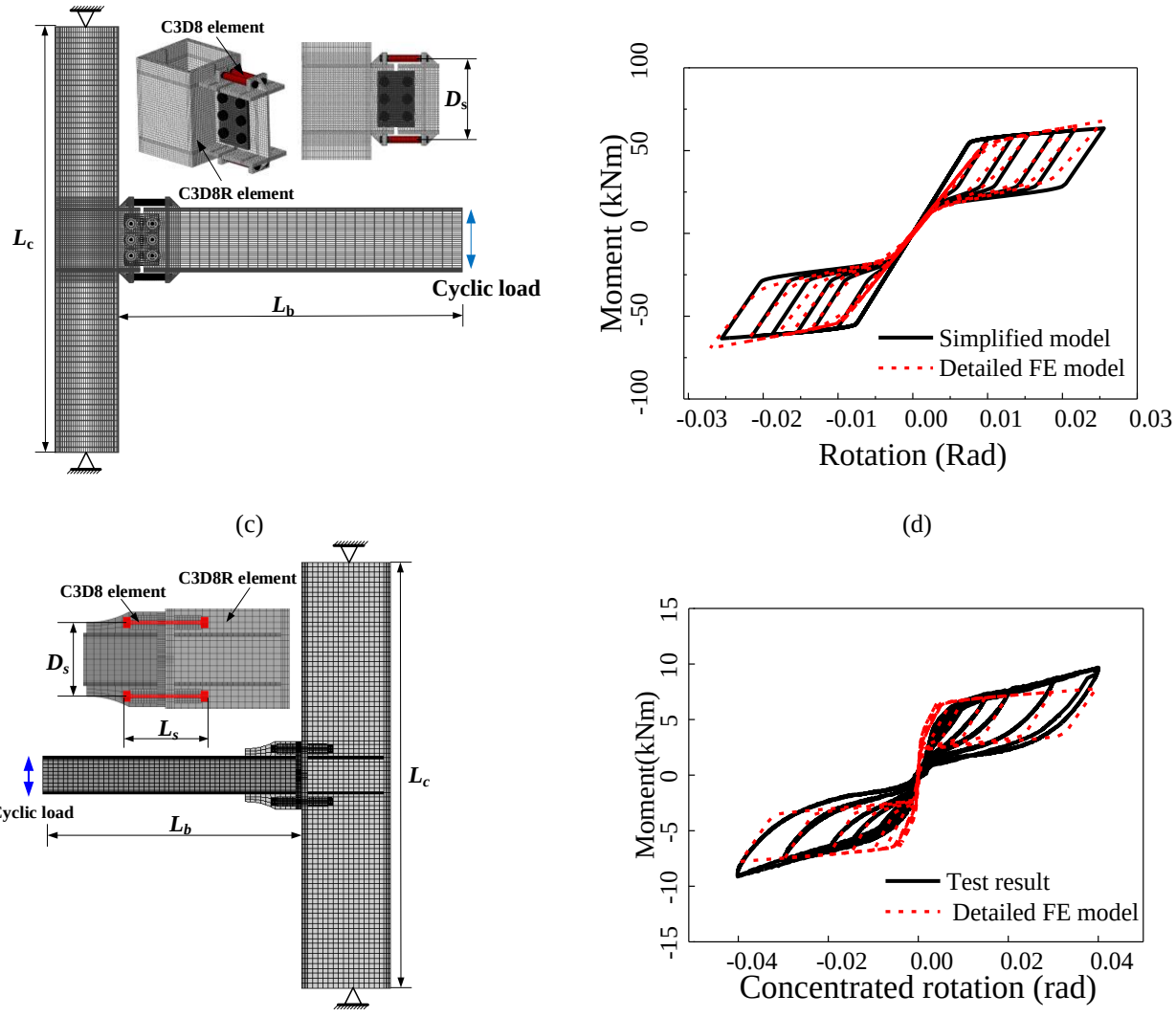

Figure 4. Connection models: (a) nonlinear-spring-based simplified model, (b) material properties of SMA bars [39], (c) detailed FE model of the proposed connection, (d) results of the proposed connection (e) detailed FE model of test connection in [39]. and (f) Results of test connection.

4. Analysis procedures and seismic response of prototype structures

4.1 Analysis procedures

The validated FE models mentioned above are used to simulate the prototype structures, and they are subjected to nonlinear cyclic pushover analysis and nonlinear response history analysis (NL-RHAs). The invariant lateral force pattern corresponding to the fundamental vibration mode is applied on the prototype structures to conduct the cyclic pushover analyses. The lateral load distribution is given as follows:

$$\mathbf{F} = \mathbf{m}\boldsymbol{\varphi}_1 \quad (1)$$

where $\mathbf{F}$ = lateral load vector corresponding to the fundamental vibration mode of the prototype structures; $\mathbf{m}$ = mass matrix; and $\boldsymbol{\varphi}_1$ = modal vector corresponding to the fundamental vibration mode. Note that a frequency analysis should be carried out first to obtain the lateral load vector, and the elastic dynamic properties of the prototype structures are summarised in table 3. To apply the invariant lateral load distribution in Eq. (1), "Equation" option in ABAQUS [46] is used to couple the applied lateral load in each storey of the systems.

The NL-RHAs are performed to examine the seismic response of prototype structures subjected to earthquake motions. Twenty earthquake ground motions utilised in the SAC project [48] are adopted as the ground motion ensemble. These ground motion data (i.e. coded from LA01 to LA20) may be reckoned as design based earthquake motions on sites of stiff soil with 10% probability of exceedance in fifty (50) years. The acceleration spectra corresponding to the damping ratio of 5% is given in figure 5. For both the

nonlinear cyclic pushover analysis and the NL-RHAs, P-delta effects are considered, and the gravity load is applied by distributing the lumped mass on each floor. In NL-RHAs, a damping ratio of 5% [49] is used to develop the Rayleigh damping matrix for the first two vibration modes.

Table 3. Dynamic properties of the prototype HSSF-SCEDBs.

Structure	Property (unit)	1^{st} Mode	$2^{nd.}$ Mode
3-storey system	Period (s)	0.70	0.22
	Modal effective mass (t)	179.54	9.64
	Modal participation factor	1.30	0.50
6-storey system (A) (L_{SMA}=75 mm)	Period (s)	1.67	0.54
	Modal effective mass (t)	466.10	77.20
	Modal participation factor	1.37	0.53
6-storey system (B) (L_{SMA}=150 mm)	Period (s)	1.90	0.62
	Modal effective mass (t)	469.21	71.99
	Modal participation factor	1.36	0.52

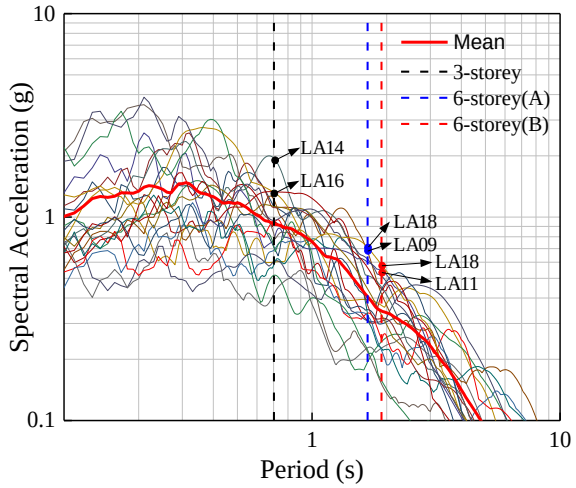

Figure 5. Acceleration spectra of earthquake motions.

4.2 Seismic response of prototype structures under earthquake motions

The cyclic pushover responses of the prototype structures in the "push" direction (up to the maximum roof drift of 4%) are shown in figure 6. For six-storey system (A) progressing into the martensite hardening stage (figure 6(b)), the response up to the roof drift where the maximum axial strain in SMA bolts reaches 8% is given, after which fracture of SMA bolts may be triggered. It can be seen that the typical flag-shape hysteretic responses with negligible residual deformation are characterised in a wide deformation range for the three prototype structures. Note that the realistic residual deformations of the structure under earthquake motions are always less than those extracted from the cyclic pushover responses [50-52]. Therefore, it is expected that the post-earthquake residual deformations of the structures may be insignificant. Evident stiffness hardening at large drift levels is observed due to the variation of mechanical characteristics of SMAs (i.e. martensite hardening). Comparing the cyclic responses of two six-storey structures (i.e. figure 6(b) and figure 6(c)), it can be observed that the variation of SMA bolt length greatly influences the cyclic response of the structure. The shorter SMA bolts in the six-storey system (A) yielded earlier than the longer SMA bolts in the six-storey system (B). This is due to the more significant axial strain in a shorter SMA bolt under the identical drift level.

The maximum interstorey drift responses of three prototype structures under the earthquake motions are shown in figure 7, and responses under individual earthquake motion accompanied with the mean responses (indicated by a blue line) are illustrated. For the three prototype structures, the maximum elongation of SMA bolts is below 8% under

the earthquake motions ensemble, and hence all the analysis results are presumed to be valid. The three-storey prototype structure undergoes the most intense interstorey drifts when subjected to earthquake motion LA14 and LA16. According to figure 5, the spectral accelerations of these two ground motions are the most significant at the period of 0.70 s, i.e. the fundamental vibration period of the three-storey structure. Thus, it appears that the seismic demands of the low-rise structure are directly related to the vibration characteristics of the fundamental vibration mode. The six-storey system (A) experiences the most significant responses under LA16, which are inconsistent with the cases with maximum spectral accelerations according to figure 5. Similar observations are characterised for the six-storey system (B). These findings imply that the inelastic demands of a medium-rise HSSF-SCEDBs are not solely dependent on the spectral acceleration at the fundamental vibration mode. A practical approach which quantifies the influential factors affecting the seismic demands of a HSSF-SCEDB will be presented in a later section.

Figure 8 gives the residual interstorey drift responses of the prototype structures under the earthquake motions. To obtain the actual residual deformation of a structure after an earthquake motion, additional analysis time is added to allow for the decay of structural vibration. It is seen that the post-earthquake residual interstorey drifts are insignificant notwithstanding that the peak interstorey drifts are generally above the codified limit (i.e. 2% [44]). In particular, the maximum residual interstorey drift of the three-storey structure subjected to twenty earthquake motions is below 0.1%, and the average post-earthquake residual interstorey drift is generally below 0.03%. As for the two six-storey structures, the maximum residual interstorey drifts are below 0.2%, and the average residual interstorey drift responses are generally close to 0.05%. Recalling that the hysteretic responses of the systems exhibit typical flag-shape without significant residual deformations for a wide deformation range (Figure 6), these results are reasonable. In contrast, it was observed from recent studies that the post-earthquake residual interstorey drifts of conventional steel moment resisting frames (MRFs) under an ensemble of design-level earthquake motions may exceed 0.5% [53]. Thus, the comparatively more encouraging post-earthquake residual deformation of a HSSF-SCEDB is confirmed.

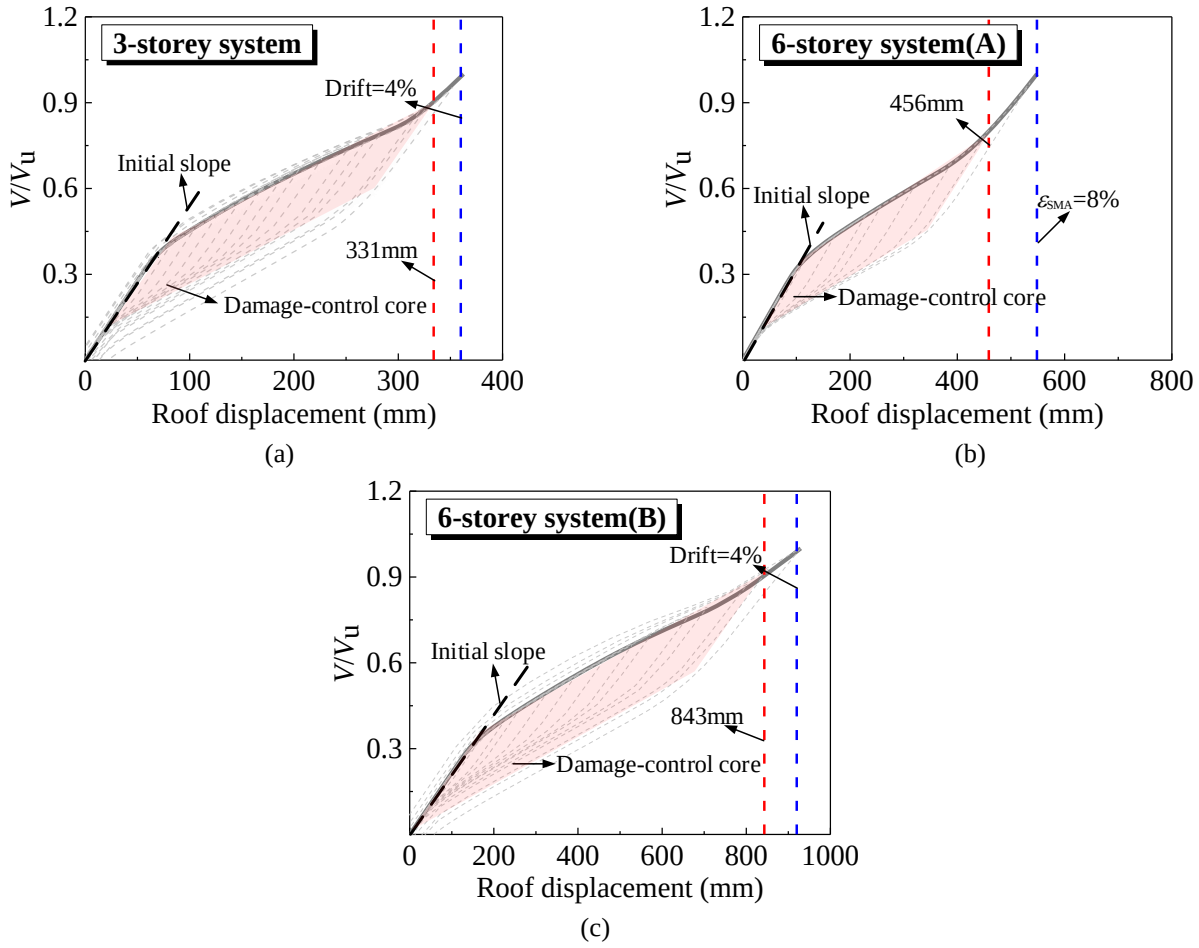

Figure 6. Cyclic pushover response of prototype structures: (a) 3-storey system, (b) 6-storey system (A) and (c) 6-storey system (B).

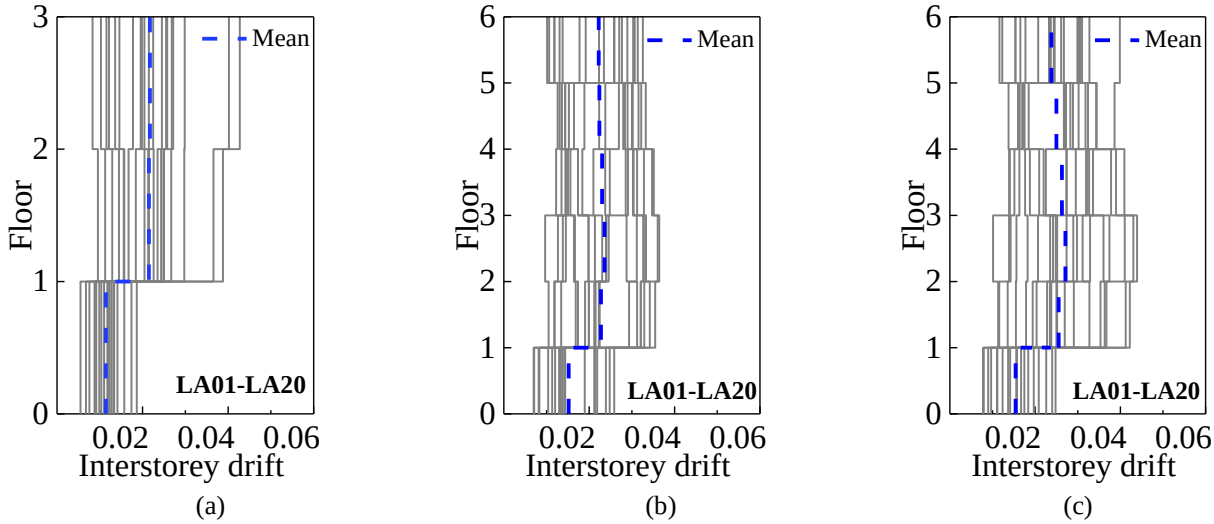

Figure 7. Maximum interstorey drifts: (a) 3-storey system, (b) 6-storey system (A) and (c) 6-storey system (B).

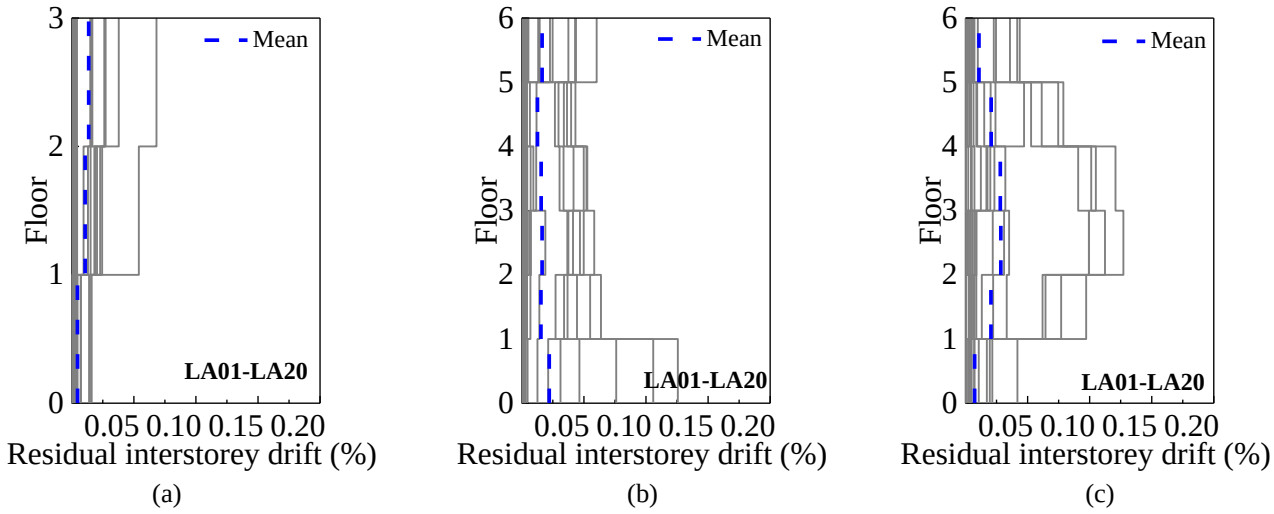

Figure 8. Residual interstorey drifts: (a) 3-storey system, (b) 6-storey system (A) and (c) 6-storey system (B).

It is of great interest to compare the responses of the six-storey system (A) and the six-storey system (B) with varied SMA bolt lengths. As shown in figure 7(b) and figure 7(c), the average peak interstorey drift and the response dispersion of the six-storey system (B) under the ground motion ensemble is more significant than that of six-storey system (A), notwithstanding that the average spectral acceleration at the fundamental vibration period of the six-storey system (A) is higher than that of the six-storey system (B). This observation indicates that the regained elasticity of SMA bolts due to "martensite hardening" in the six-storey system (A) at large deformation levels may contribute to mitigating the peak deformation demand of the system. Similarly, the corresponding residual interstorey drift of the six-storey system (A) is smaller than that of the six-storey system (B). However, special caution needs to be exercised if a structure is expected to deform into the martensite hardening stage, because SMA bolts are exposed to risks of brittle failure when subjected to large deformations. In summary, the peak responses and the post-earthquake residual interstorey drifts under the ground motions ensemble confirm the potential of HSSF-SCEDB structures for resilient seismic engineering application.

5. Multi-mode-based nonlinear static procedure for quantifying damage-control behaviour and estimating seismic demands of HSSF-SCEDBs

5.1 Basic assumption

The proposed procedure is developed based on a fundamental presumption that the seismic responses of a multi-storey HSSF-SCEDB may be estimated using equivalent modal single-degree-of-freedom (SDF) systems. The basic assumptions are listed as follows:

(1) The inelastic seismic demand of a HSSF-SCEDB can be quantified by suitable superposition of demands of equivalent modal SDF systems considering essential modes, and the coupling effect among modal SDF systems induced by inelasticity of the system is ignored.

(2) The equivalent modal SDF system corresponding to higher vibration modes of a HSSF-SCEDB deforms in the elastic range.

(3) The skeleton pushover response curve of a HSSF-SCEDB can be reasonably approximated by a trilinear idealisation, and a "damage-control core" formed by a "flag" with significant post-yielding stiffness ratio can be utilised to characterise the hysteretic behaviour of the system deforming in the damage-control stage.

It is emphasised that the motive of adopting the first two assumptions is to produce a practical tool for practitioners, and trade-offs between theoretical rigorousness and practical simplicity are made. Nonetheless, the adequacy of the two assumptions in seismic evaluations has been examined thoroughly by Chopra and colleagues in studies on modal pushover analysis [54-56]. The rationale and limitation of the assumptions for evaluating the seismic demand of HSSF-SCEDBs will be studied in detail in later sections.

5.2 Seismic energy balance of a damage-control HSSF-SCEDB

Based on the first basic assumption, the seismic demand of a HSSF-SCEDB can be estimated using an equivalent modal SDF system. As schematically shown in figure 9, an inelastic SDF oscillator following the typical flag-shape hysteretic law [57-59] is used to characterise the fundamental mode of a HSSF-SCEDB deforming in the damage-control stage. A modified energy balance equation [60, 61] based on the classical Housner principle [62] is utilised to quantify the seismic demand of a HSSF-SCEDB as follows:

$$\gamma(\frac{1}{2}mS_{\mathrm{v}}^2) = E_{\mathrm{a}} \tag{2}$$

where m = mass of the SDF oscillator, S_{v} = spectral pseudo-velocity, E_{a} = the nominal absorbed energy determined as the covered area between the nonlinear skeleton pushover response and the horizontal axis (figure 9), and γ = energy factor of a flag-shape SDF system defined by the ratio of E_{a} to the absorbed energy of the correlated elastic SDF system with the identical elastic vibration properties (i.e. E_{ae} in figure 9) under an earthquake motion. The energy factor of a flag-shape SDF system [63] can be expressed by:

$$\gamma = \chi(T;\xi;\mu_{\mathrm{s}};\alpha;\beta)[2\mu_{\mathrm{s}} - 1 + \alpha(\mu_{\mathrm{s}} - 1)^2] \tag{3}$$

$$\chi = \frac{V_{\mathrm{y}}^2(T;\xi;\mu_{\mathrm{s}};\alpha;\beta)}{V_{\mathrm{e}}^2(T;\xi)} \tag{4}$$

where χ = damage-control factor, α = post-yield stiffness ratio of the system in the damage-control stage (i.e. the ratio of the post-yield stiffness in the damage-control stage to the elastic stiffness of the system as shown in figure 9), β = energy ratio determined as the ratio of the height of the "flag" to the yield strength (V_{y}), μ_{s} = ductility quantified by the ratio of the maximum inelastic displacement (δ_{T}) to the equivalent yield displacement of SCEDBs (δ_{y1}), T = period of the system and ξ = damping ratio. Note that a constant-ductility-based method [63, 64] may be used to compute the energy factor of a flag-shape SDF system. Comparatively, an elastic SDF system is used to account for the higher vibration modes affecting the seismic response of the structure (assumption 2), in which case the energy factor equals unity.

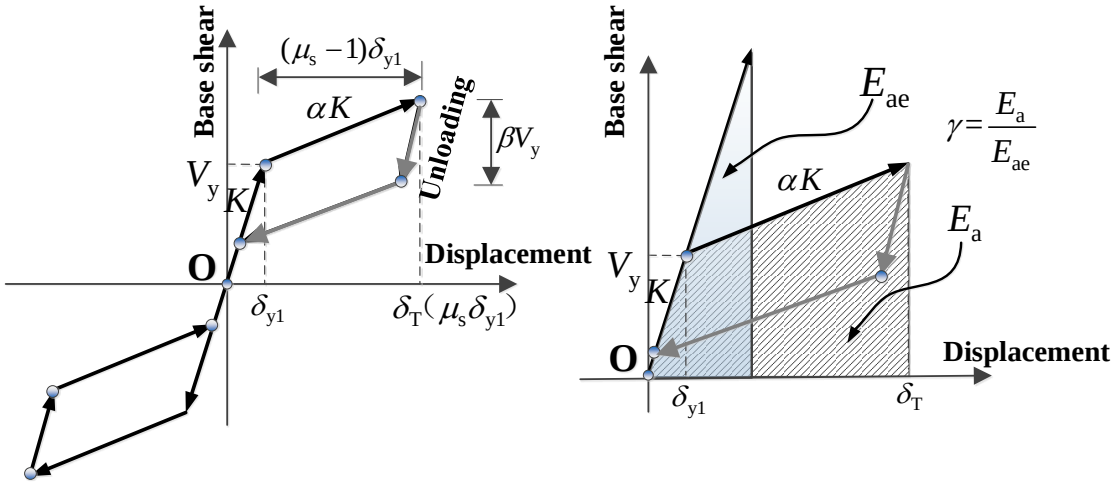

Figure 9. Hysteretic rule and energy balance of the system in the damage-control stage.

5.3 Multi-mode-based nonlinear static procedure

A stepwise procedure is developed based on the energy balance of modal equivalent SDF systems, and given as follows:

Step 1: Perform frequency analysis and determine the elastic vibration properties of a HSSF-SCEDB considering critical vibration modes, namely the natural period T_n, the effective mass M_n^*, the modal participation factor Γ_n, and the modal vector $\boldsymbol{\varphi}_n$. It is recommended that the sum of effective masses of the considered modes should exceed 90% of the seismic mass of the entire system. Thus, for typical frame structures, the first two or three vibration modes may suffice.

Step 2: Conduct modal cyclic pushover analyses for the fundamental mode and modal monotonic pushover analysis for the higher vibration modes. The lateral load distributions corresponding to higher vibration modes given as follows can be combined with Eq. (1)

$$\mathbf{F}_n = \mathbf{m}\boldsymbol{\varphi}_n \tag{5}$$

where $\mathbf{F}_n$ = pushover load vector of the higher modes (n= 2, 3…). In this step, the P-Δ effect should be considered by including the influence of the gravity load.

Step 3: The HSSF-SCEDB is idealised as equivalent modal SDF systems considering influential modes. Specifically, an energy-based method proposed by Hernandez-Montes et al. [65], which may effectively eliminate the "reversal phenomenon" of response curves observed in a conventional force-based pushover method, is used to develop the "energy-based pushover response curves" and "nominal energy capacities" for the equivalent modal SDF systems. Based on "assumption (1)" in Section 5.1, the equivalent energy-based modal SDF systems are developed respectively by ignoring interactions among multi-vibrations triggered by inelasticity. Therefore, the absorbed energy of an equivalent modal SDF system based on the skeleton pushover response can be quantified using an incremental approach:

$$\Delta E_n^k = \frac{1}{2}(\mathbf{F}_n^{k-1} + \mathbf{F}_n^k)\cdot(\boldsymbol{\delta}_n^k - \boldsymbol{\delta}_n^{k-1}) \tag{6}$$

$$E_n^k = E_n^{k-1} + \Delta E_n^k \tag{7}$$

where ΔE_n^k = incremental absorbed energy of an equivalent SDF system at the "**k**th" step for the "**n**th" mode and $\boldsymbol{\delta}_n$ = lateral displacement profile. Meanwhile, as the absorbed energy by the equivalent SDF system for the "**n**th" mode in a differential displacement Δu_{en} is equal to the work done by the lateral loads of the "**n**th" mode, the incremental energy-based displacement [65, 66] of the "**k**th" step for the "**n**th" mode can be obtained using the pushover database, given by

$$\Delta u_{en}^k = \frac{2\Delta E_n^k}{V_{bn}^k + V_{bn}^{k-1}} \tag{8}$$

$$u_{en}^k = u_{en}^{k-1} + \Delta u_{en}^k \tag{9}$$

where $\boldsymbol{V}_{bn}$ = the force of an equivalent SDF system for the "**n**th" mode, given by

$$V_{bn} = \mathbf{F}_n \cdot \mathbf{1} \tag{10}$$

Therefore, the energy-based skeleton pushover responses can be developed by plotting the base shear against the energy-based displacement, and the nominal energy capacity curves can be generated by plotting the absorbed energy against the energy-based displacement. More detailed derivation of generating energy-based SDF systems can be found in [65, 66].

Step 4: Idealise the skeleton pushover responses (i.e. base shear versus energy-based displacement curves) of the fundamental vibration mode by a multi-linear simplification based on a target displacement, which is given by

$$V = \begin{cases} ku & 0 \le u \le u_1 \\ \alpha ku + (1-\alpha)ku_1 & u_1 < u \le u_2 \\ \alpha ku + (\alpha-\eta)ku_2 + (1-\eta)ku_1 & u_2 < u \end{cases} \tag{11}$$

where k = initial slope of the pushover curve, u_1 = displacement corresponding to the first inflexion point in the multi-linear idealisation, u_2 = displacement corresponding to the second inflexion point in the multi-linear idealisation, α = post-yielding stiffness ratio of the damage-control stage, and η = post-yielding stiffness ratio of the post-damage-control stage. A least-square-based algorithm proposed by Ke and Chen [15] can be used to determine the multi-linear idealisation. The governing equations for the simplification are reproduced as follows:

$$\begin{aligned} \varpi(k,u_1,u_2,\alpha,\eta) = &\sum_{i=1}^{A}(ku_i - f_i)^2 + \sum_{i=A+1}^{A+B}[\alpha k(u_i-u_1) + ku_1 - f_i)]^2 \\ &+ \sum_{i=A+B+1}^{A+B+C}[\eta k(u_i-u_2) + \eta k(u_2-u_1) + ku_1 - f_i)]^2 \end{aligned} \tag{12}$$

where A = data point number in the elastic range; B = data point number in the first post-yielding stage (i.e. damage-control stage) and C = data point number in the second post-yielding stage (i.e. post-damage-control stage). u_i = displacement corresponding to the "**i**th" data point, f_i = force corresponding to the "**i**th" data point. Therefore, the trilinear idealisation can be finalised when $\varpi(k,u_1,u_2,\alpha,\eta)$ reaches the minimum. The deformation corresponding to the second inflexion point may be used to quantify the boundary of the "damage-control core". It is worth noting that yielding of the HSS frame leads to stiffness reduction at large displacement, whereas "martensite hardening" of SMA at large deformations enhances the stiffness. Thus, the second inflexion point in the trilinear idealisation does not necessarily quantify a specific performance point (e.g. yielding inception of the HSS frame or initiation of martensite hardening of SMA bolts) due to the combined effect mentioned above.

Step 5: Quantify the hysteretic parameters (α, β and μ_s) of the damage-control core (i.e. the flag) using the cyclic pushover curves of the fundamental vibration mode up to the second inflexion point defined as the deformation threshold. In particular, bilinear idealisation documented in FEMA 273 [67] can be used to idealise the skeleton pushover curve.

Step 6: Determine the energy demand given by

$$D=\begin{cases}\gamma(T;\xi;\mu_s;\alpha;\beta)\dfrac{1}{2}M_1 S_1^2(T_1) & \text{n}=1\\ \dfrac{1}{2}M_n S_{vn}^2(T_n) & \text{n}>1\end{cases} \quad (13)$$

where S_{v1} = spectral pseudo-velocity corresponding to the fundamental mode, S_{vn} = spectral pseudo-velocity corresponding to the "**n**th" vibration mode, M_1 = effective mass of the fundamental vibration mode, and M_n = effective mass of the "**n**th" vibration mode. For each vibration mode, generate the energy demand curve by plotting the energy demand against the energy-based displacement.

Step 7: Correlate the energy capacity curve with the corresponding demand curve for each mode, respectively. In cases where an intersection of the capacity and demand is achieved below the defined deformation threshold for the first mode, it is predicted that the damage-control behaviour of the system can be achieved. Otherwise, it is expected that the structure will progress into the post-damage-control stage. In cases where the structure deforms in the damage-control stage, the peak response demand of the "nth" mode is computed based on the intersecting point of the energy demand curve and the corresponding capacity curve. Specifically, response demand quantities (e.g. peak roof drift and maximum interstorey drift) may be determined from the pushover data pool when modal oscillators deform to the "intersecting point". The peak response demand of the entire HSSF-SCEDB is estimated by "SRSS" superposition rule [54-56], given as follows:

$$R=\left(\sum_{n=1}^{i} r_n^2\right)^{0.5} \quad (14)$$

where R = peak response of a damage-control HSSF-SCEDB and r_n = response demand of a modal SDF system considering the "**n**th" mode. In general, the procedure integrates the energy-based procedure [60-62, 65, 66] and the practical attractiveness of the modal pushover procedure [54-56].

6. Implementation of the procedure

6.1 Damage-control evaluations

The multi-mode-based nonlinear static procedure is used to evaluate the damage-control behaviour of the prototype HSSF-SCEDBs subjected to earthquake motions. The skeleton pushover curves of the prototype structures corresponding to the fundamental vibration mode up to the maximum interstorey drift of 4% or the deformation corresponding to the maximum SMA bolt elongation of 8%, are extracted and shown in figure 10. The roof displacements corresponding to the deformation threshold (i.e. the second inflexion point) are also indicated in figure 6.

The energy factor demands of the prototype structures considering the fundamental vibration mode are computed, and the results for the twenty earthquake motions accompanied with the mean value are plotted against the energy-based displacement as shown in figure 11. A damping ratio of 5% is used to be consistent with NL-RHA of the structural systems. Unlike the case of conventional HSSF-EDBs in which the energy factor generally decreases with increasing inelastic deformations under most earthquake motions [17], special cautions should be exercised in scenarios where the energy factor significantly increases with the energy-based displacement.

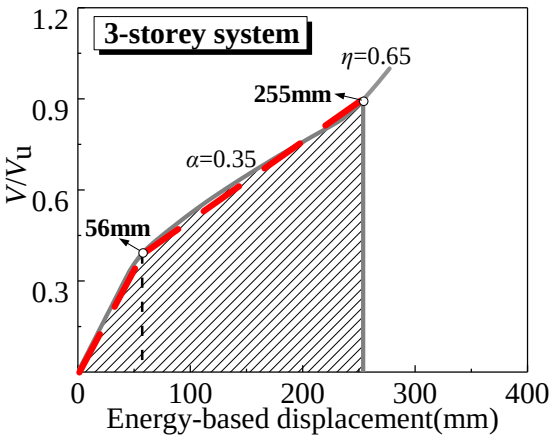

(a)

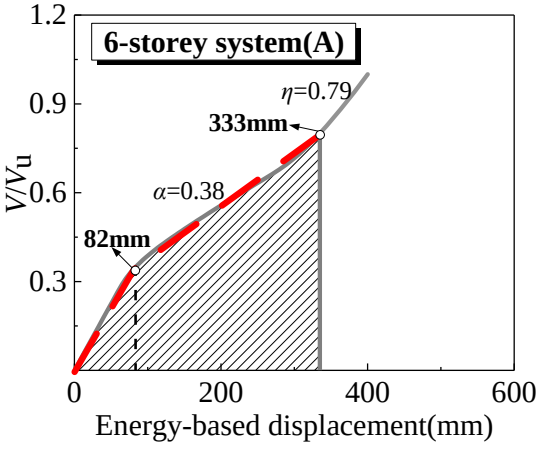

(b)

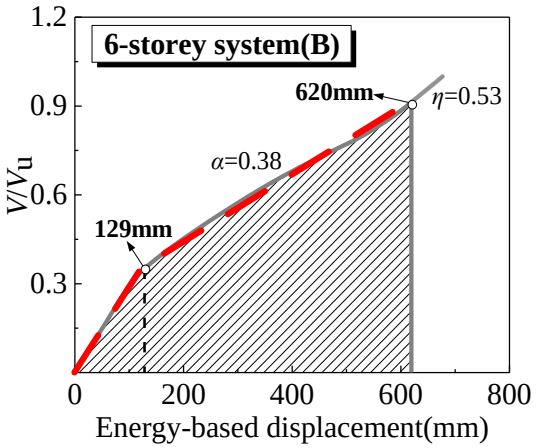

(c)

Figure 10. Energy-based pushover responses of the fundamental mode: (a) 3-storey system, (b) 6-storey system (A) and (c) 6-storey system (B).

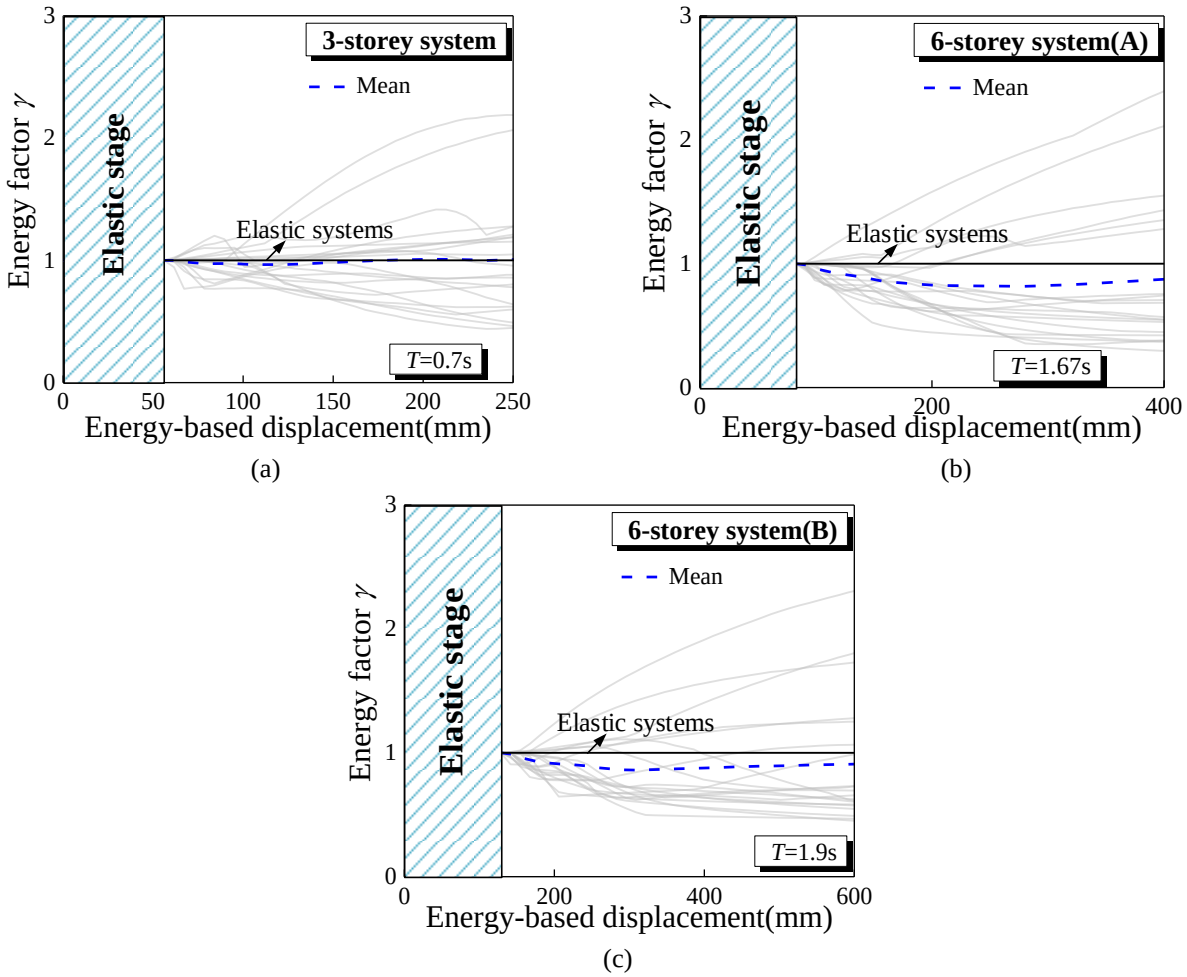

(a) (b)

(c)

Figure 11. Energy factor demand of the fundamental mode: (a) 3-storey system, (b) 6-storey system (A) and (c) 6-storey system (B).

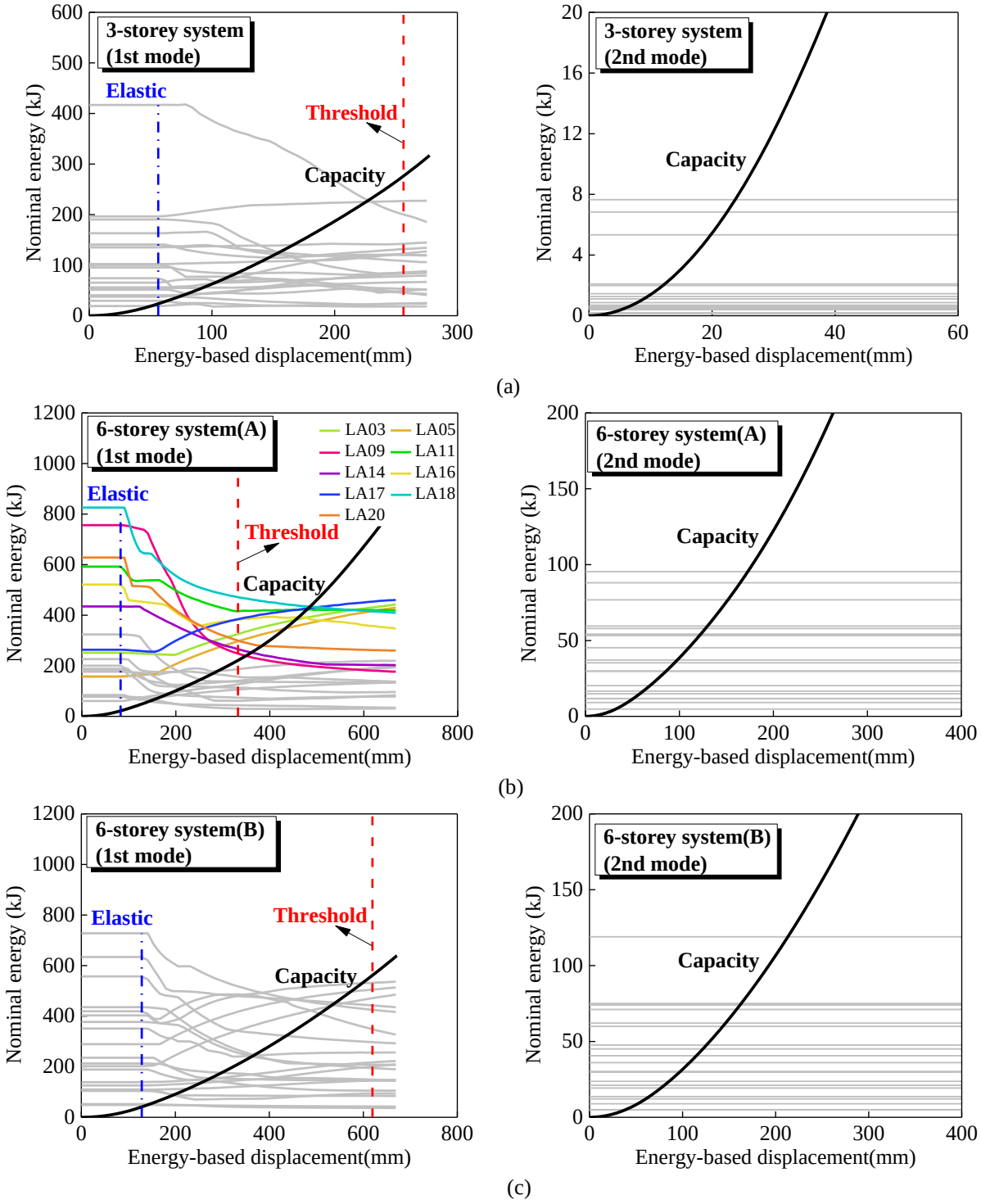

Figure 12. Demand and capacity responses: (a) 3-storey system, (b) 6-storey system (A) and (c) 6-storey system (B).

The energy capacity curves (step 3) and energy demand curves (step 6) are compared, as shown in figure 12. Thus, the six-storey system (A) is expected to progress to the post-damage-control stage under ground motion LA03, LA05, LA09, LA11, LA14, LA16, LA17, LA18 and LA20, as the intersecting points cannot be achieved before the selected deformation threshold. The effectiveness of the procedure can be justified through comparing the peak roof displacement by NL-RHAs and the defined threshold given in figure 13. Note that the roof displacement threshold corresponds to the second inflexion point of energy-based pushover responses. As can be seen, the procedure is able to successfully capture all earthquake motions that push the structures to the defined post-damage-control stage.

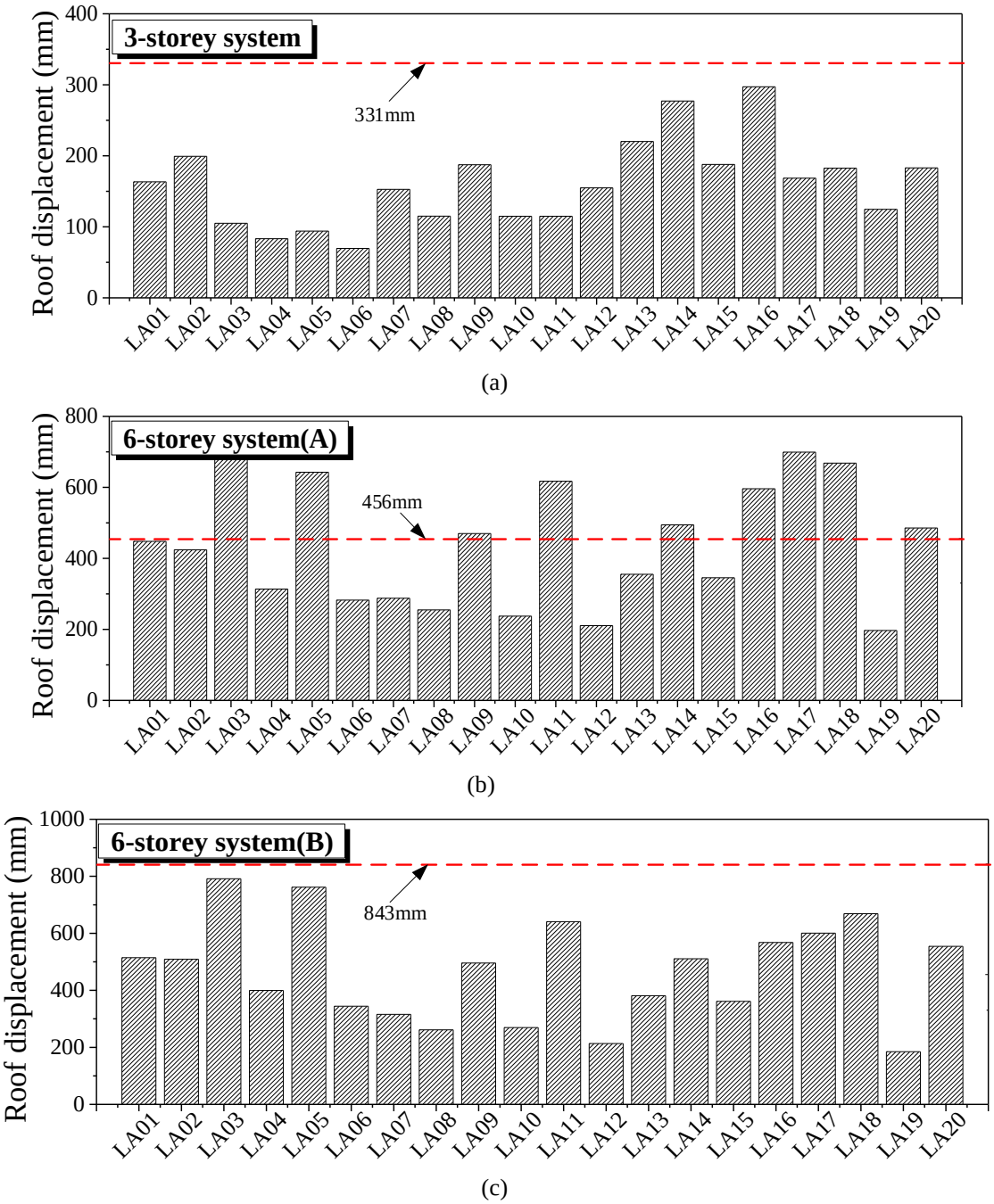

Figure 13. Roof displacement of prototype structures: (a) 3-storey system, (b) 6-storey system (A) and (c) 6-storey system (B).

6.2 Estimation of seismic demands

The seismic demand of the three prototype structures deforming in the damage-control stage is estimated following the stepwise procedure discussed in Section 5.3. The first two vibration modes are considered in the multi-mode-based nonlinear static procedures. For comparison, the demand response quantities based on the fundamental vibration mode are computed. In this case, the demand curves are determined using only the effective mass considering the fundamental mode of the system (M_1). In addition, recent studies show that the behaviour of a low-to-medium rise structure may be reasonably simulated by a fundamental-mode-based SDF oscillator with the mass of the entire structure [61]. Thus, the seismic demand is also estimated using a fundamental-mode-based SDF system lumped with the mass of the entire structure (M) in this study.

The roof displacement and the interstorey drift are used to examine the accuracy of the proposed procedure. In particular, δ_{MNSP} denotes the roof displacement predicted by

the proposed multi-mode-based nonlinear static procedure, and prediction by NL-RHA is represented by $\delta_{\text{NL-RHA}}$. The maximum interstorey drift predicted by NL-RHA is represented by $\theta_{\text{NL-RHA}}$, and the counterpart determined from the multi-mode-based static procedure is represented by θ_{MNSP}. Thus, the effectiveness of the multi-mode-based nonlinear static procedure for predicting the structural seismic demands of a damage-control HSSF-SCEDB can be quantified by the ratio of the response quantities determined by the nonlinear static procedures to that of NL-RHAs (i.e. the roof displacement ratio and the maximum interstorey drift ratio), given by

$$\delta^*_{\text{MNSP}} = \frac{\delta_{\text{MNSP}}}{\delta_{\text{NL-RHA}}} \tag{15}$$

$$\theta^*_{\text{MNSP}} = \frac{\theta_{\text{MNSP}}}{\theta_{\text{NL-RHA}}} \tag{16}$$

The peak roof displacements estimated by the approximate procedures are plotted against the counterparts by NL-RHAs, as shown in figure 14. For a comparative study, predictions based on the effective mass considering the fundamental mode is represented by $\delta_{\text{NSP}(M1)}$, and the mass of the entire structure is represented by $\delta_{\text{NSP}(M)}$. The results show that the data points are clustered near the forty-five-degree diagonal line, and the predictions based on the entire mass of the structure are more conservative compared with the other two methods. The average ratio δ^*_{MNSP} and the corresponding coefficient of variation (CoV) considering the ground motion ensemble are indicated in figure 14, and the promise for the multi-mode-based nonlinear static procedure for quantifying the roof displacement of a damage-control HSSF-SCEDB is confirmed.

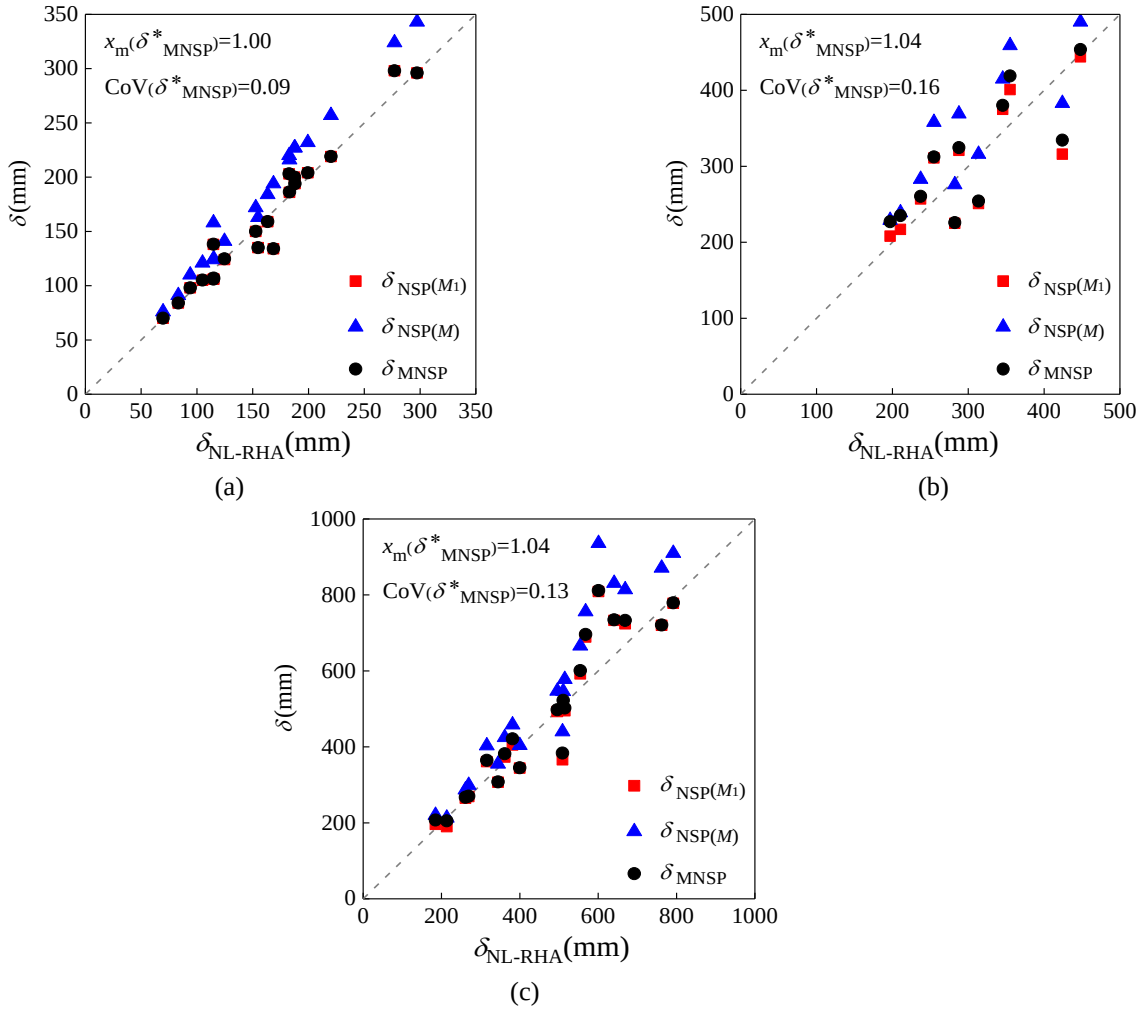

Figure 14. Roof displacement demands: (a) 3-storey system, (b) 6-storey system (A) and (c) 6-storey system (B).

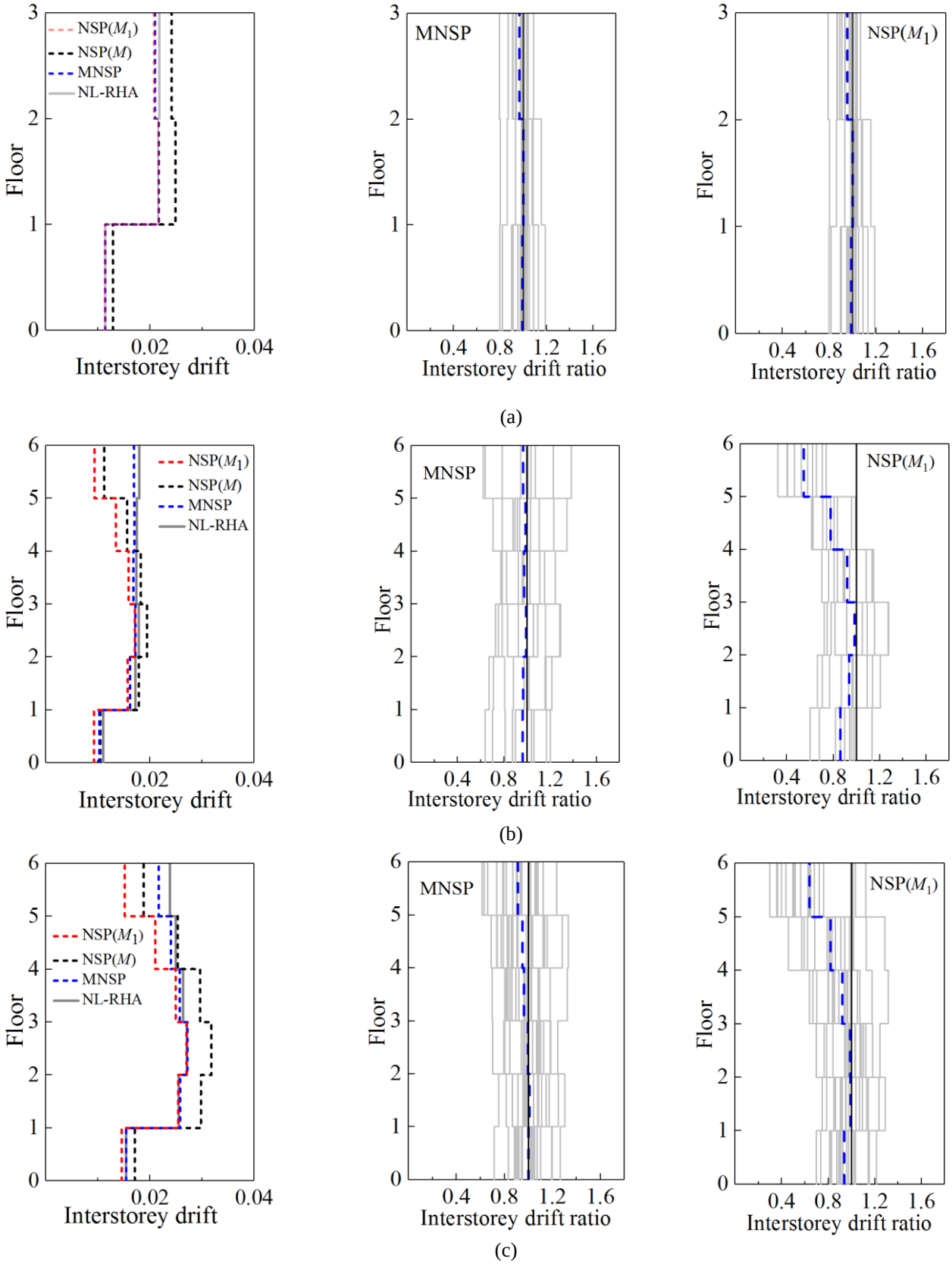

Figure 15. Interstorey drift demands: (a) 3-storey system, (b) 6-storey system (A) and (c) 6-storey system (B).

The maximum interstorey drift and the interstorey drift ratio are given in figure 15. The interstorey drift and the interstorey drift ratios based on the MNSP using SRSS superposition and based on the effective mass of the fundamental mode (M_1) are also shown. As shown in the figure, there is negligible difference between the predictions by the multi-mode-based nonlinear static procedure using SRSS superposition and those based on the effective mass of the fundamental mode (M_1) for the three-storey structure. This is expected since the influence of higher vibration modes on the structure is minimal in this case. Comparatively, the interstorey drift over all storeys is slightly overestimated using the mass of the entire structure. For the two six-storey structures, it is observed that the three approximate procedures generally result in reasonable estimates of the interstorey drift demands of the systems in lower storeys, whereas the demands estimated by the multi-mode-based nonlinear static procedure show enhanced accuracy in upper storeys. The comparison of interstorey drift ratios based on multi-modes and those based on the fundamental modes also implies that the higher vibration modes may appreciably influence the inelastic seismic demands of a medium-rise HSSF-SCEDB. This is also echoed by recent research works on novel self-centring systems showing typical flag-shape hysteresis [68]. In this context, the proposed procedure is a promising tool for damage-control evaluation and seismic demand quantification of HSSF-SCEDBs affected by higher vibration modes.

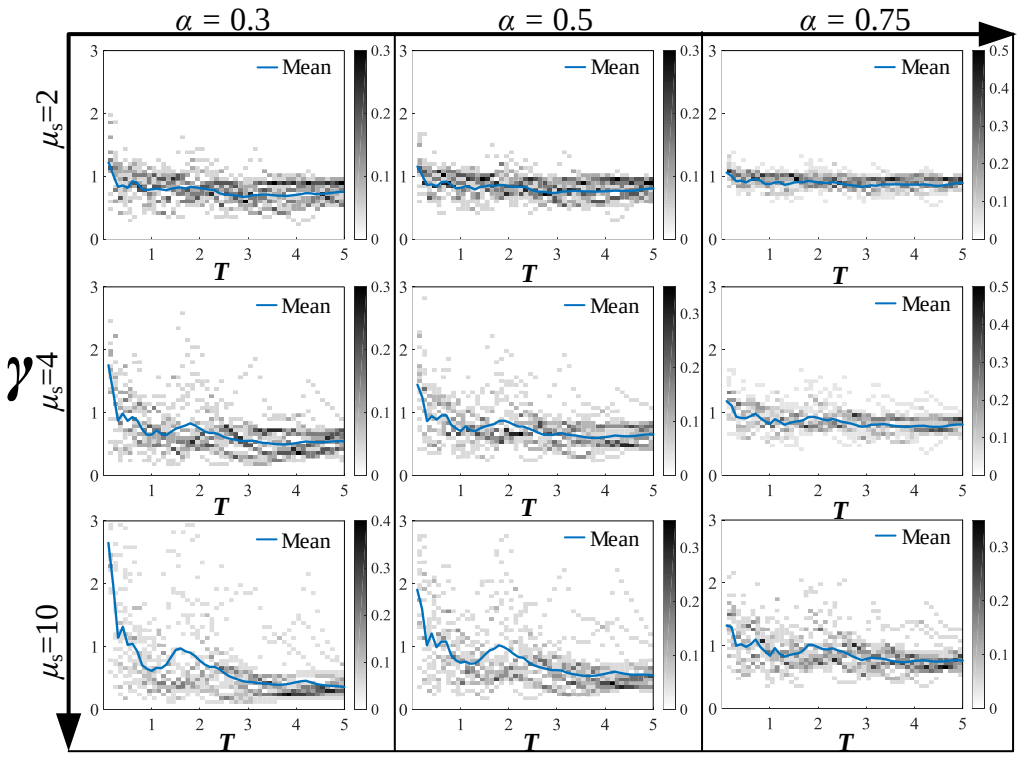

Figure 16. Representative energy factor spectra.

6.3 Further analyses and discussions

Computation of the energy factor demand is a basis for assessing the damage-control behaviour and quantifying the seismic demand of the representative SDF oscillators. In this study, further spectral analyses of flag-shape SDF systems are performed to demonstrate the effect of the hysteretic parameters and vibration properties on the energy factor demand of the system.

Representative energy factor spectra of flag-shape SDF oscillators covering a spectrum of hysteretic parameters and periods under the earthquake motions (i.e. LA01-LA20) are shown in figure 16. Thus, the period-dependency of the energy factor and the influence of hysteretic parameters can be confirmed. The statistical distribution of the energy factor of SDF systems under twenty earthquake motions is also indicated by a frequency contour in figure 16 to clarify the dispersion of the data. As a general remark, the dispersion of the energy factor is decreased with increasing α, whereas increases with increasing μ_s. Therefore, the energy factor demand can be further adjusted by changing the structural arrangement of a HSSF-SCEDB. For instance, if a large

deformation range is expected for the damage-control stage, a correspondingly high post-yielding stiffness ratio is preferred using a stiffer HSS frame. In this respect, the proposed procedure may offer a physical base towards an in-depth interpretation of the interaction between earthquake motion characteristics and nonlinear structural dynamic features of a damage-control HSSF-SCEDB. Notwithstanding the advantages of the proposed procedure, ignoring the coupling effect among multi-vibration modes of the system could result in inconsistent prediction of the seismic demands. This limitation can also be seen by revisiting the predicted demands under individual ground motion, as given in figure 15, which has also been observed in previous works on modal pushover analysis procedures [54-56]. Thus, the proposed multi-mode-based nonlinear static procedure may not be applicable for predicting demands of a damage-control HSSF-SCEDB subjected to individual earthquake motions.

7. Conclusions

A proof-of-concept study to enhance the high strength steel (HSSF) moment resisting frames using self-centring energy dissipation bays (SCEDBs) equipped with superelastic shape memory alloy (SMA) connections is conducted. The seismic performance of prototype structures is examined by pushover analysis and nonlinear response history analysis (NL-RHAs) using a set of earthquake motions. The damage-control behaviour of the system and essential seismic demand indices including the maximum interstorey drifts and post-earthquake residual interstorey drift are examined in detail. A multi-mode-based nonlinear static procedure motivated by the modified energy balance principle is developed enabling seismic demands evaluation of the novel structure subjected to expected earthquake motions. The essential findings and conclusions are drawn as follows:

(1) The prototype HSSF-SCEDBs exhibit multi-yielding stages under hysteretic loading scenarios, and a damage-control core characterised by flag-shape hysteresis with significant post-yielding stiffness ratio can be extracted from the responses curves. The comparison between the two structures with varied connection design but identical structural arrangement confirms that the hysteretic characteristics of the damage-control core can be readily modulated by adjusting the connection detail (e.g. the length of the SMA bolts in the connection).

(2) The NL-RHA results of the prototype structures offered evidence that the HSSF- SCEDBs can achieve encouraging recentring behaviour with negligible post-earthquake residual deformations even after experiencing peak deformations beyond the codified deformation threshold (i.e. 2% documented in current Chinese seismic provisions [44]).

(3) The nonlinear dynamic seismic responses of a HSSF-SCEDB is sensitive to the structural behaviour of the SMA connections. The maximum interstorey responses of the systems imply that the uncertainty of inelastic seismic demands of the structures subjected to earthquake motions might be amplified by a damage-control core with wider deformation spectrum (i.e. a wider plateau of the "flag").

(4) Good agreement between the seismic demand quantity predictions of the prototype structures by the multi-mode-based nonlinear static procedure and those by the NL- RHAs confirms the adequacy of the method for evaluating the damage-control behaviour of a HSSF-SCEDB and quantifying the peak seismic demands of the system (e.g. peak roof displacement and maximum interstorey drift). The comparison between the seismic demands by the proposed procedure considering multi-modes and those by the fundamental mode highlighted the influence of higher vibration modes on a medium-rise HSSF-SCEDB.

(5) The energy factor spectra of oscillators representing damage-control HSSF-SCEDBs covering a wider spectrum of parameters show that the seismic demands of a damage-control HSSF-SCEDB can be adjusted by modulating the structural arrangement to achieve preferable nonlinear characteristics.

(6) Statistical analysis results of the energy factor show that increasing the target ductility leads to more evident dispersion of the seismic demand quantities, but an increasing post-yielding stiffness ratio in the damage-control stage contributes to mitigating this effect, which can be realised by enhancing the lateral stiffness of HSS frames.

Acknowledgements

This research is financially supported by the National Natural Science Foundation of China (Grant No. 51890902 and 51708197) and the Research Grants Council of the Hong Kong Special Administrative Region, China with Grant No. PolyU 152096/19E. The authors would also like to thank Chinese National Engineering Research Centre for Steel Construction, The Hong Kong Polytechnic University (Project No. 1-BBV4) for providing funding support. The assistance of Mr Qun He in numerical analysis of the prototype connection and his advice in improving the connection detail is acknowledged.

References

[1] Bjorhovde R 2004 Development and use of high performance steel *J. Constr. Steel Res.* **60** 393-400

[2] Aslani F, Uy B, Tao Z and Mashiri F 2015 Behaviour and design of composite columns incorporating compact high-strength steel plates *J. Constr. Steel Res.* **107** 94-110

[3] Shi G, Wang M, Bai Y, WangF, Shi Y and Wang Y 2012 Experimental and modeling study of high-strength structural steel under cyclic loading *Eng. Struct.* **37** 1-13
[4] Wang YB, Li GQ, Cui W, Chen SW and Sun FF 2015 Experimental investigation and modeling of cyclic behavior of high strength steel *J. Constr. Steel Res.* **104** 37-48
[5] Hu F and Shi G 2018 Constitutive model for full-range cyclic behavior of high strength steels without yield plateau *Constr. Build. Mater.* **162** 596-607
[6] Hai LT, Sun FF, Zhao C, Li GQ and Wang YB 2018 Experimental cyclic behavior and constitutive modeling of high strength structural steels *Constr. Build. Mater.* **189** 1264-1285
[7] Sousa ADC and Nussbaumer A 2019 Multiaxial ultra low cycle fatigue in welded high strength steel structural components *J. Constr. Steel Res.* **153** 473-482
[8] Wang YB, Li GQ, Cui W and Chen SW 2014 Seismic behavior of high strength steel welded beam-column members *J. Constr. Steel Res.* **102** 245-255
[9] Pucinotti R, Tondini N, Zanon G and Bursi OS 2015 Tests and model calibration of high-strength steel tubular beam-to-column and column-base composite joints for moment-resisting structures *Earthq. Eng. Struct. Dyn.* **44** 1471-1493
[10] Atlayan O and Charney FA 2014 Hybrid buckling-restrained braced frames *J. Constr. Steel Res.* **96** 95-105
[11] Dubina D, Stratan A and Dinu F 2018 Dual high-strength steel eccentrically braced frames with removable links *Earthq. Eng. Struct. Dyn.* **37** 1703-1720
[12] Tenchini A, D'Aniello M, Rebelo C, Landolfo R, Da Silva LS and Lima L 2016 High strength steel in chevron concentrically braced frames designed according to Eurocode 8 *Eng. Struct.* **124** 167-185
[13] Wang F, Su M, Hong M, Guo Y and Li S 2016 Cyclic behaviour of Y-shaped eccentrically braced frames fabricated with high-strength steel composite *J. Constr. Steel Res.* **120** 176-187
[14] Hu F, Shi G and Shi Y 2017 Experimental study on seismic behavior of high strength steel frames: Global response *Eng. Struct.* **131** 163-179
[15] Ke K and Chen Y 2016 Seismic performance of MRFs with high strength steel main frames and EDBs *J. Constr. Steel Res.* **126** 214-228
[16] Chen Y and Ke K 2019 Seismic performance of high-strength-steel frame equipped with sacrificial beams of non-compact sections in energy dissipation bays *Thin-Walled. Struct.* **139** 169-185
[17] Ke K, Yam MCH, Deng L and Zhao Q 2018 A modified DEB procedure for estimating seismic demands of multi-mode-sensitive damage-control HSSF-EDBs *J. Constr. Steel Res.* **150** 329-345
[18] Ke K, Wang W, Yam MCH and Deng L 2019 Residual displacement ratio demand of oscillators representing HSSF-EDBs subjected to near-fault earthquake ground motions *Eng. Struct.* **191** 598-610
[19] Tian X, Su M, Lian M, Wang F and Li S 2018 Seismic behavior of K-shaped eccentrically braced frames with high-strength steel: shaking table testing and FEM analysis *J. Constr. Steel Res.* **143** 250-263
[20] Connor JJ, Wada A, Iwata M and Huang YH 1997 Damage-controlled structures. I: Preliminary design methodology for seismically active regions *J. Struct. Eng.* **123** 423-431
[21] Ke K and Yam MCH 2018 A performance-based damage-control design procedure of hybrid steel MRFs with EDBs *J. Constr. Steel Res.* **143** 46-61
[22] Lopes AP 2016 Seismic behavior and design of the linked column steel frame system for rapid return to occupancy The Portland State University *(Portland, Oregon)*
[23] Shen Y L, Christopoulos C, Mansour N and Tremblay R 2011 Seismic design and performance of steel moment-resisting frames with nonlinear replaceable links *J. Struct. Eng.* **137** 1107-1117
[24] Christopoulos C, Tremblay R, Kim HJ and Lacerte M 2008 Self-centering energy dissipative bracing system for the seismic resistance of structures: development and validation *J. Struct. Eng.* **134** 96-107
[25] Iyama J, Seo CY, Ricles JM and Sause R 2009 Self-centering MRFs with bottom flange friction devices under earthquake loading *J. Constr. Steel Res.* **65** 314-325
[26] Wolski M, Ricles JM and Sause R 2009 Experimental study of a self-centering beam-column connection with bottom flange friction device *J. Struct. Eng.* **135** 479-488
[27] DesRoches R, Mccormick J and Delemont M 2004 Cyclic properties of superelastic shape memory alloy wires and bars *J. Struct. Eng.* **130** 38-46
[28] Fang C, Yam MCH, Ma H and Chung KF 2015 Tests on superelastic Ni-Ti SMA bars under cyclic tension and direct-shear: towards practical recentring connections *Mater. Struct.* **48** 1013-1030
[29] Wang W, Fang C and Liu J 2016 Large size superelastic SMA bars: heat treatment strategy, mechanical property and seismic application *Smart Mater. Struct.* **25** 75001
[30] Seo J, Kim YC and Hu JW 2015 Pilot study for investigating the cyclic behavior of slit damper systems with recentering shape memory alloy (SMA) bending bars used for seismic restrainers *Applied Sci.* **5** 187-208
[31] Seo J and Hu JW 2016 Seismic response and performance evaluation of self-centering LRB isolators installed on the CBF building under NF ground motions *Sustainability*. **8** 109
[32] Seo J, Hu JW and Kim KH 2017 Analytical investigation of the cyclic behavior of smart recentering T-Stub components with superelastic SMA bolts *Metals.* **7** 386
[33] Ocel J, DesRoches R, Leon RT, Hess WJ, Krumme R, Hayes JR and Sweeney S 2004 Steel beam-column connections using shape memory alloys *J. Struct. Eng.* **130** 732-740
[34] Speicher MS. DesRoches R and Leon RT 2011 Experimental results of a NiTi shape memory alloy (SMA)-based recentering beam-column connection *Eng. Struct.* **33** 2448-2457
[35] Wang W, Fang C and Liu J 2017 Self-centering beam-to-column connections with combined superelastic SMA bolts and steel angles *J. Struct. Eng.* **143** 04016175
[36] Fang C, Wang W, Ricles J, Yang Y, Zhong Q, Sause R and Chen Y 2018 Application of an innovative SMA ring

spring system for self-centering steel frames subject to seismic conditions *J. Struct. Eng.* **144** 04018114

[37] Wang W, Fang C, Yang X, Chen Y, Ricles J and Sause R 2017 Innovative use of a shape memory alloy ring spring system for self-centering connections *Eng. Struct.* **153** 503-515

[38] Fang C, Wang W, He C and Chen Y 2017 Self-centring behaviour of steel and steel-concrete composite connections equipped with NiTi SMA bolts *Eng. Struct.* **150** 390-408

[39] Fang C, Yam MCH, Chan TM, Wang W, Yang X and Lin X 2017 A study of hybrid self-centring connections equipped with shape memory alloy washers and bolts *Eng. Struct.* **164** 155-168

[40] DesRoches R, Taftali B and Ellingwood BR 2010 Seismic performance assessment of steel frames with shape memory alloy connections. Part I- Analysis and seismic demands *J. Earthq. Eng.* **14** 471-486

[41] Sultana P and Youssef MA 2016 Seismic performance of steel moment resisting frames utilizing superelastic shape memory alloys *J. Constr. Steel Res.* **125** 239-251

[42] Qiu C, Li H, Ji K, Hou H and Tian L 2017 Performance-based plastic design approach for multi-story self-centering concentrically braced frames using SMA braces *Eng. Struct.* **153** 628-638

[43] McCormick J, DesRoches R, Fugazza D and Auricchio F 2007 Seismic assessment of concentrically braced steel frames with shape memory alloy braces *J. Struct. Eng.* **133** 862-870

[44] GB50011-2010 2010 *Code for Seismic Design of Buildings* (Beijing, China: Chinese Building Press)

[45] GB5009-2012 2012 *Load code for Design of Buildings* (Beijing, China: Chinese Building Press)

[46] ABAQUS Standard, Version 6.12 2012 *ABAQUS Analysis User's Manual*

[47] Auricchio F, Coda A, Reali A and Urbano M 2009 SMA numerical modeling versus experimental results: parameter identification and model prediction capabilities *J. Mater. Eng. Perform.* **18** 649-54

[48] Somerville P 1997 Development of ground motion time histories for phase 2 of the FEMA/SAC steel project *SAC* Background Document SAC/BD-91/04 (*Sacramento, Calif: SAC Joint Venture)*

[49] Vargas R and Bruneau M 2009 Experimental response of buildings designed with metallic structural fuses. II *J. Struct. Eng.* **135** 394-403

[50] MacRae GA and Kawashima K 1997 Post earthquake residual displacements of bilinear oscillators *Earthq. Eng. Struct. Dyn.* **26** 701-716

[51] Guo WWJ and Christopoulos C 2013 A procedure for generating performance spectra for structures equipped with passive supplemental dampers *Earthq. Eng. Struct. Dyn.* **42** 1321-1338

[52] Guo WWJ and Christopoulos C 2017 A probabilistic framework for estimating the residual drift of idealized SDOF systems of non-degrading conventional and damped structures *Earthq. Eng. Struct. Dyn.* **47** 479-796

[53] Erochko J, Christopoulos C, Tremblay R and Choi H 2011 Residual drift response of SMRFs and BRB frames in steel buildings Designed according to ASCE 7-05 *J. Struct. Eng.* **137** 589-599

[54] Chopra AK and Goel RK 2002 A modal pushover analysis procedure for estimating seismic demands for buildings *Earthq. Eng. Struct. Dyn.* **31** 561-582

[55] Chintanapakdee C and Chopra AK 2003 Evaluation of modal pushover analysis using generic frames *Earthq. Eng. Struct. Dyn.* **32** 417-442

[56] Chopra AK, Goel RK and Chintanapakdee C 2004 Evaluation of a modified MPA procedure assuming higher modes as elastic to estimate seismic demands *Earthq. Spectra.* **20** 757-778

[57] Christopoulos C, Filiatrault A and Folz B 2002 Seismic response of self-centring hysteretic SDOF systems *Earthq. Eng. Struct. Dyn.* **31** 1131-1150

[58] Karavasilis TL and Seo C 2011 Seismic structural and non-structural performance evaluation of highly damped self-centering and conventional systems *Eng. Struct.* **33** 2248-2258

[59] Zhou Y, Song G, Huang S and Wu H 2019 Input energy spectra for self-centering SDOF systems *Soil Dyn. Earthq. Eng.* **121** 293-305

[60] Lee SS, Goel SC and Chao SH 2001 Performance-based design of steel moment frames using target drift and yield mechanism *Research Report No. UMCEE 01-17 (Department of Civil and Environmental Engineering, University of Michigan, Ann Arbor, Michigan)*

[61] Leelataviwat S, Saewon W and Goel SC 2009 Application of energy balance concept in seismic evaluation of structures *J. Struct. Eng.* **135** 113-121

[62] Housner GW 1956 Limit design of structures to resist earthquakes *In: Proceeding of the 1st WCEE*

[63] Ke K, Chuan G and Ke S 2016 Seismic energy factor of self-centering systems subjected to near-fault earthquake ground motions *Soil Dyn. Earthq. Eng.* **84** 169-173

[64] Zhai C, Ji D, Wen W, Lei W and Xie L 2016 Constant ductility energy factors for the near-fault pulse-like ground motions *J. Earthq. Eng.* **21** 343-358

[65] Hernandez-Montes E, Kwon OS and Aschheim MA 2004 An energy-based formulation for first- and multiple-mode nonlinear static (pushover) analyses *J. Earthq. Eng.* **8** 69-88

[66] Jiang Y, Li G and Yang D 2010 A modified approach of energy balance concept based multimode pushover analysis to estimate seismic demands for buildings *Eng. Struct.* **32** 1272-1283

[67] Federal Emergency Management Agency 1997 NEHERP provisions for the rehabilitation of buildings FEMA No.273 (Guidelines) and 274 (Commentary) *(Washington, DC)*

[68] Qiu CX and Zhu S 2016 High-mode effects on seismic performance of multi-story self-centering braced steel frames *J. Constr. Steel Res.* **119** 133-143

Appendix A

The rationality of using the modelling techniques for reproducing the behaviour of HSS members can be verified using a large-scale test on a HSS frame made of Q460 steel. Moment versus drift responses of representative joints gleaned from the test database are compared with FE predictions, as shown in figure A1. The symbols of the joints are shown in figure A2. A reader may refer to [15] for detailed information on the experimental programme.

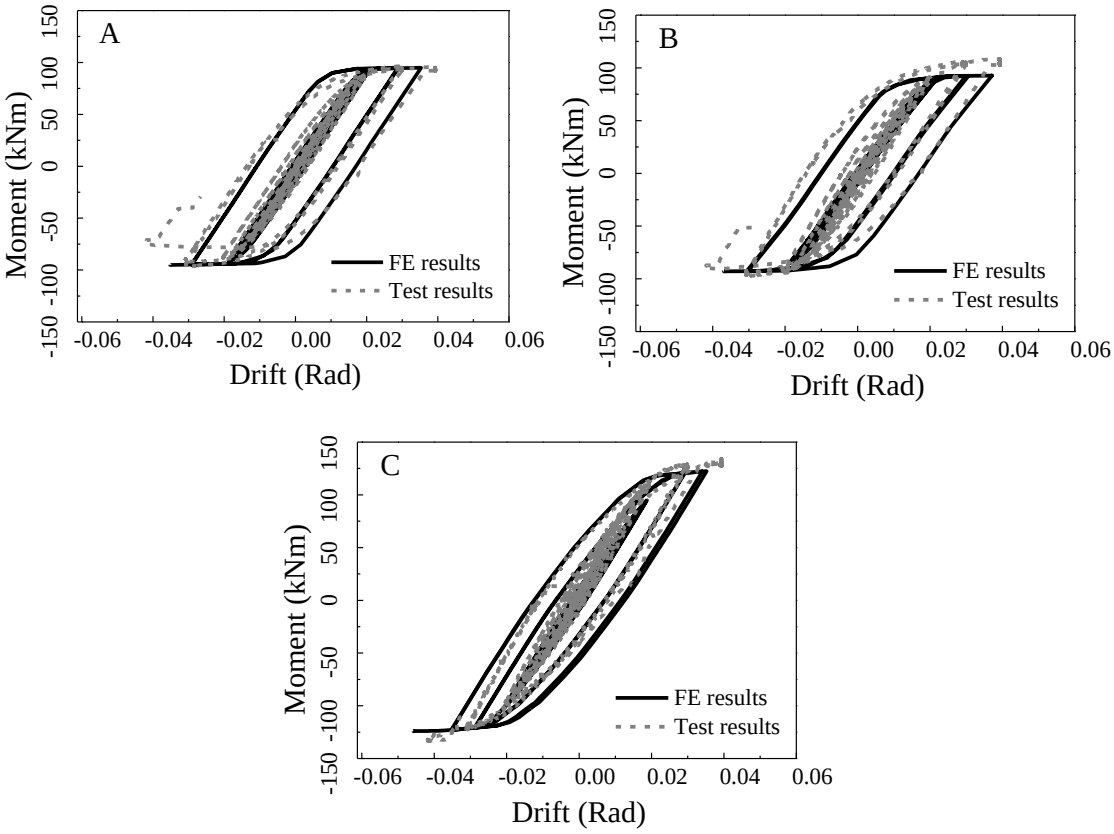

Figure A1. Comparison between test results of HSS frames [15] and FE predictions.

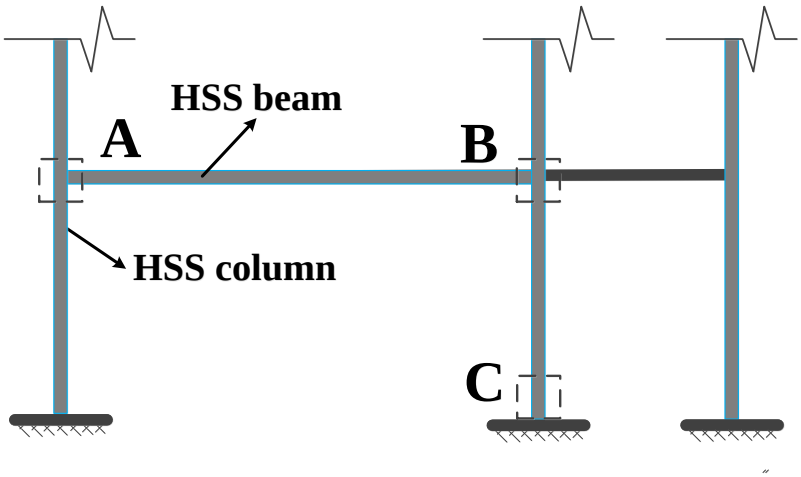

Figure A2. Location and designation of joints.